Recent methane surges reveal heightened emissions from tropical inundated areas

X. Lin[1*], S. Peng[2], P. Ciais[1,3] , D. Hauglustaine[1], X. Lan[4,5], G. Liu[2], M. Ramonet[1], Y. Xi[1,2], Y. Yin[6], Z. Zhang[7], H. Bösch[8,9], P. Bousquet[1], F. Chevallier[1], B. Dong[2], C. Gerlein-Safdi[10], S. Halder[1], R. J. Parker[8,9], B. Poulter[11], T. Pu[10], M. Remaud[1], A. Runge[12], M. Saunois[1], R. L. Thompson[13], Y. Yoshida[14], B. Zheng[15,16]

[1]Laboratoire des Sciences du Climat et de l'Environnement, LSCE/IPSL, CEA-CNRS-UVSQ, Université Paris-Saclay, Gif-sur-Yvette, France

[2]Sino-French Institute for Earth System Science, College of Urban and Environmental Sciences, Peking University, Beijing, China

[3]Climate and Atmosphere Research Center (CARE-C), The Cyprus Institute, Nicosia, Cyprus

[4]Cooperative Institute for Research in Environmental Sciences of University of Colorado, Boulder, CO, USA

[5]Global Monitoring Laboratory, National Oceanic and Atmospheric Administration, Boulder, CO, USA

[6]Division of Geological and Planetary Sciences, California Institute of Technology, Pasadena, CA, USA

[7]National Tibetan Plateau Data Centre, State Key Laboratory of Tibetan Plateau Earth System, Environment and Resource, Institute of Tibetan Plateau Research, Chinese Academy of Sciences, Beijing, China

[8]National Centre for Earth Observation, Space Park Leicester, University of Leicester, Leicester, UK

[9]Earth Observation Science, School of Physics and Astronomy, University of Leicester, Leicester, UK

[10]Department of Civil and Environmental Engineering, University of California, Berkeley, CA, USA

[11]Biospheric Sciences Laboratory, NASA Goddard Space Flight Center, Greenbelt, MD, USA

[12]Alfred Wegener Institute, Helmholtz Centre for Polar and Marine Research, Potsdam, Germany

[13]Norwegian Institute for Air Research (NILU), Kjeller, Norway

[14]National Institute for Environmental Studies, Tsukuba, Japan

[15]Institute of Environment and Ecology, Tsinghua Shenzhen International Graduate School, Tsinghua University, Shenzhen, China

[16]State Environmental Protection Key Laboratory of Sources and Control of Air Pollution Complex, Beijing, China

[*] To whom correspondence may be addressed: Xin Lin (xin.lin@lsce.ipsl.fr)

This is a non-peer reviewed preprint that has been submitted to *Nature Communications*.

Abstract

Record breaking atmospheric methane growth rates were observed in 2020 and 2021 (15.2±0.4 and 17.6±0.5 ppb yr^{-1}), reaching their highest level since the commencement of ground-based observations in the early 1980s. Here we use an ensemble of atmospheric inversions informed by surface or satellite methane concentration observations to infer emission changes during these two years relative to 2019. We found a global increases of methane emissions of 20.3±9.9 Tg CH_4 in 2020 and 24.8±3.1 Tg CH_4 in 2021. The emission rise was dominated by tropical and boreal regions with inundated areas, as a result of elevated groundwater table. Strong, synchronous, and persistent emission increases occurred in regions such as the Niger River basin, the Congo basin, the Sudd swamp, the Ganges floodplains and Southeast Asian deltas and the Hudson Bay lowlands. These regions alone contributed about 70% and 60% of the net global increases in 2020 and 2021, respectively. Comparing our top-down estimates with simulation of wetland emissions by biogeochemical models, we find that the bottom-up models significantly underestimate the intra- and inter-annual variability of methane sources from tropical inundated areas. This discrepancy likely arises from the models' limitations in accurately representing the dynamics of tropical wetland extents and the response of methane emissions to environmental changes. Our findings demonstrate the critical role of tropical inundated areas in the recent surge of methane emissions and highlight the value of integrating multiple data streams and modeling tools to better constrain tropical wetland emissions.

Main

In the years 2020 and 2021, the methane growth rate (MGR) in the atmosphere reached 15.2±0.4 and 17.6±0.5 parts per billion per year (ppb yr^{-1}) respectively, hitting record high since systematic measurements started in early 1980s by NOAA's Global Monitoring Laboratory (GML) (Lan et al., 2023; https://gml.noaa.gov/ccgg/trends_ch4/). The unprecedented methane growth during 2020 and 2021 coincided with the reduced human activities and pollutant emissions during COVID-19 lockdowns and the gradual recovery afterwards (Davis et al., 2022; Jackson et al., 2022; Laughner et al., 2021; Miyazaki et al., 2021), together with the occurrence of a moderate and prolonged La Niña event (Li et al., 2022; https://psl.noaa.gov/enso/mei/), which offers a unique opportunity to examine the drivers of methane variabilities on a year-to-year basis.

Both process-based studies of sources ("bottom-up" estimates) and atmospheric-based inverse analyses ("top-down" estimates) pointed to pronounced emission growth in 2020 compared to 2019, arising from tropical and northern sources, likely driven by enhanced wetland emissions (Feng et al., 2023; Peng et al., 2022; Qu et al., 2022; Zhang et al., 2023), the main source component of natural methane emissions. This is consistent with the overall earlier and larger increase of MGR observed in the Tropics and Northern high-latitudes than Southern extra-tropics from marine boundary layer sites of the surface network (Fig. 1b; Supplementary Fig. 1). The exceptionally high methane growth occurred again in 2021 over most latitude bands, although followed by a drop in MGR towards the end of the year (Fig. 1a, b). Observations of total column methane concentrations (XCH_4) by Greenhouse Gases Observing SATellite (GOSAT), whether obtained from the National Institute for Environmental Studies (Japan) full physics retrievals (hereafter "GSNIES"; Inoue et al., 2016) or from the University of Leicester proxy retrievals (hereafter "GSUoL"; Parker et al., 2020), confirmed the unexpected methane surge in 2020 and 2021 (Fig. 1c, d). Note that both GOSAT retrievals showed a larger increase in MGR over Southern extra-tropics than that observed from surface network, with GSUoL exhibiting higher MGR globally and in the Tropics as well (Fig. 1; Supplementary Fig. 1).

The zonally-averaged changes in MGR reveal the integrated variations of regional sources and sinks, atmospheric transport, and removal by OH. To infer the spatiotemporal patterns in flux changes from 2019 to 2021, we applied three-dimensional (3D) atmospheric inversions using an inversion system PYVAR-LMDZ-SACS that assimilated either surface or satellite-based

CH_4 observations. An ensemble of six inversions was performed using the same inversion setup, but different in assimilated observation datasets (surface network, GSNIES or GSUoL) and transport model physical parameterizations (the "classic" and "standard" versions) (Supplementary Table 1; see Methods). This allows us to test the consistency of flux change patterns inferred from different types of measurements while accounting for some of the uncertainties due to imperfect representation of atmospheric mixing. Surface networks offer a good coverage of northern mid-to-high latitudes (especially over Europe and North America), whereas satellite data have improved data densities from 60°S to 60°N, including the tropics (Supplementary Figs. 2 & 3). We prescribed changes in OH concentration fields simulated from a full chemistry transport model LMDZ-INCA (Hauglustaine et al., 2004, 2014), driven by interannually varying meteorology from ECMWF ERA5 reanalysis (Hersbach et al., 2018) with natural and anthropogenic emissions of NO_x, CO and hydrocarbons updated to 2021 that account for reductions and rebound of NO_x and CO emissions by anthropogenic activities and changes in wildfires (Carbon Monitor; Community Emissions Data System (CEDS); van der Werf et al., 2017). Our chemistry transport model LMDZ-INCA simulated a reduction of global tropospheric OH by 3% in 2021 relative to 2019, more than the 1.6–1.8% decrease in 2020 as reported by Peng et al. (2022) (Supplementary Fig. 4 & Table 2).

The ensemble of six inversions showed global increases in surface CH_4 emissions by an average of 20.3±9.9 Tg CH_4 yr^{-1} and 24.8±3.1 Tg CH_4 yr^{-1} in 2020 and 2021 respectively, compared to 2019. A large portion of this surge in global emissions was accounted for by the northern tropics (0°–30°N), which contributed about 80% (16.2±8.3 Tg CH_4 yr^{-1}) and 95% (23.2±4.0 Tg CH_4 yr^{-1}) of the global increases in 2020 and 2021, respectively (Fig. 2a, b; Supplementary Fig. 5 & Table 3). Strong emission increases were consistently found over tropical Africa and Southeast Asia in both years, according to all six inversions (Fig. 2a, b; Supplementary Figs. 5–7). Overall, most of the regions with strong and consistent emission changes overlap with major wetland complexes and inundated areas. These trends align well with changes in Gravity Recovery and Climate Experiment Follow-On (GRACE-FO) liquid water equivalent (LWE) height anomalies (Fig. 2, Supplementary Fig. 5), a proxy for water-table depth and water stored in wetland systems (Bloom et al., 2010).

Focusing on 20 major wetland regions that represent about 60% of global wetland areas based on the regularly flooded wetland map of Tootchi et al. (2019), a significant correlation was noted between top-down estimates of emission anomalies and changes in LWE from GRACE-

FO (Fig. 2). Notably, the Niger River basin, the Congo basin, the Sudd swamp, the Ganges floodplains and Southeast Asian deltas in the tropics, and the Hudson Bay lowlands in the boreal region, exhibited persistent emission enhancements in response to increased LWE. Emission increases over each of these regions were at least 1.5–2 times the interannual variability (1.5–2σ) of methane emissions during 2010–2019, based on a former study that also used the inversion system PYVAR-LMDZ-SACS and GSUoL as constraints for CH_4 (Zheng et al., 2019). The six wetland regions together contributed around 70% (14.1±4.2 Tg CH_4 yr^{-1}) and 60% (14.9±2.6 Tg CH_4 yr^{-1}) of the global emission increases for 2020 and 2021, respectively (Fig. 2 & Fig. 3e, f; Supplementary Fig. 5 & Table 4). The strong and synchronous emission increases over these inundated regions were also coincident with the occurrence of La Niña (Li et al., 2022), which supports previous findings that showed enhanced wetland emissions in the tropics and boreal North America during historical La Niña periods (Hodson et al., 2011; Pandey et al., 2017; Zhu et al., 2017). Other regions, such as the western Siberian lowlands in 2020 and the Amazon Basin and the Orinoco floodplain in 2021, also show substantial emission increases, but reduced emissions were seen in the other year over these regions, aligning with corresponding variations in LWE. Conversely, the Pantanal and the Paraná floodplains in central and southeastern South America exhibited consistent reduction in emissions in both 2020 and 2021, likely due to continued drier conditions and lower water tables (Fig. 2; Supplementary Fig. 5 and Table 4).

Bottom-up inventories and process-based wetland emission models corroborate increased emissions over the northern tropics during 2020–2021, albeit with much smaller magnitudes than inversions (Fig. 2 & 3; Supplementary Fig. 8 and Table 3). Globally, the net emission changes were -0.7±4.0 Tg CH_4 yr^{-1} and 6.9±4.1 Tg CH_4 yr^{-1} in 2020 and 2021 relative to 2019 based on bottom-up methodologies, with emission increases of 3.2±1.3 Tg CH_4 yr^{-1} and 4.1±1.9 Tg CH_4 yr^{-1} estimated for the northern tropics (Fig. 3a, b; Supplementary Fig. 8 and Table 3). A breakdown into different processes showed that the anthropogenic CH_4 emissions in 2020 and 2021 were higher than the 2019 level by 0.5 Tg CH_4 yr^{-1} and 4.7 Tg CH_4 yr^{-1}, respectively (Fig. 3a, b; Supplementary Fig. 8 and Table 3). The global fire CH_4 emissions declined in 2020 by 6.5 Tg CH_4 yr^{-1} relative to 2019, mainly contributed by reduced fire emissions of 5.1 Tg CH_4 yr^{-1} in the southern tropics (30°S–0°) (van der Werf et al., 2017). A similar reduction of fire emissions occurred again in the southern tropics in 2021, but the extreme fires in boreal North America and eastern Siberia during the hotter and drier summertime (Zheng et al., 2023) led to an increase in emissions of 4.7 Tg CH_4 yr^{-1} in the northern extra-tropics and therefore a net global emission reduction of only 1.8 Tg CH_4 yr^{-1} relative to 2019 (Fig. 3a, b; Supplementary Fig. 8 and Table 3). For wetlands, an ensemble of process-based wetland model simulations from ORCHIDEE-MICT and LPJ-wsl driven by four different climate forcings (see Methods) reported an increase in global wetland emissions by 5.3±4.0 Tg CH_4 yr^{-1} in 2020 compared to 2019, which was dominated by enhanced wetland emissions in the northern extra-tropics and tropics as a result of warmer and wetter climate (Peng et al., 2022). The updated simulations showed slightly smaller wetland emission increases by 4.0±4.1 Tg CH_4 yr^{-1} in 2021 compared to 2019, with similar latitudinal patterns (Fig. 3a, b; Supplementary Figs. 8 & 9 and Table 3).

Given the spread of simulated wetland emissions (Supplementary Fig. 9), the total emission increases from bottom-up estimates were only 7.4 Tg CH_4 yr^{-1} and 14.4 Tg CH_4 yr^{-1} in 2020 and 2021 if the maximum increase of wetland emissions were considered, which are still 12.9 Tg CH_4 yr^{-1} and 10.4 Tg CH_4 yr^{-1} below the mean of the inversion ensemble estimates. While there was a general agreement in the broad spatial patterns of emission changes between the two methodologies, large discrepancies were found over the topics. The strong and persistent emission increases in tropical Africa and Asia, as inferred from atmospheric CH_4 observations, were consistently underestimated by bottom-up estimates (Fig. 2 & 3; Supplementary Fig. 8). Specifically, for the Niger River basin, the Congo basin, the Sudd swamp, the Ganges floodplains and Southeast Asian deltas, the bottom-up estimates of emission increases were only about 11% and 5% of the estimates from top-down inversions (Fig. 3e, f; Supplementary Table 4).

The lower bottom-up estimates of emission increases over tropical Africa and Asia inundated areas suggest that biogeochemical models substantially underestimate emissions from these water-logged ecosystems in response to changes in water-table depth and moisture conditions. Indeed, a close look into a tropical wetland emission hotspot, the Sudd swamp in the eastern Africa (3°N–17°N, 25°E–40°E; see also Lunt et al., 2019, 2021; Pandey et al., 2021) showed that the annual variations in top-down CH_4 emissions and GRACE-FO LWE anomalies were highly correlated (Supplementary Fig. 10; see also Lunt et al., 2019), implying a strong impact of water-table depth on seasonal emissions. The annual peak of LWE occurs during September–October, about one month preceding the annual peak of emissions averaged across top-down inversions. In contrast, the seasonal maximum emissions during September–

November in Sudd (about 0.3 Tg CH_4 month^{-1} relative to April–June) were coarsely underestimated by most process-based wetland simulations (giving only a non-significant rise of 0.02 Tg CH_4 month^{-1} during September–November relative to April–June; Supplementary Fig. 10). This could be partly explained by the simulation of too small wetland extents of the Sudd swamp and weak intra- and inter-annual variations, as shown by the comparison with those derived from the satellite-based CYGNSS inundated areas (Supplementary Fig. 11; Gerlein-Safdi et al., 2021). The weaker seasonal changes in wetland extent and associated CH_4 emissions were also identified previously for process-based or data-driven biogeochemical models over tropical regions (Pandey et al., 2021; Parker et al., 2018, 2022), resulting in smaller estimates of year-to-year emission anomalies. On the other hand, large uncertainties remain in the model representation of CH_4 production, oxidation and vegetation-mediated transport processes for tropical wetlands (Pangala et al., 2017; Shaw et al., 2022), where direct flux measurements are sparse (Delwiche et al., 2021; Helfter et al., 2022).

In summary, based on both ground-based and satellite-based atmospheric methane observations, we infer that surface methane emissions increased by 20.3±9.9 Tg CH_4 yr^{-1} and 24.8±3.1 Tg CH_4 yr^{-1} in 2020 and 2021 respectively, compared to 2019. The emission increases were primarily driven by a few major wetland complexes and inundated areas in the tropics and boreal regions as a result of elevated groundwater table. Strong, persistent and synchronous emission increases were found over the Niger River basin, the Congo basin, the Sudd swamp, the Ganges floodplains and Southeast Asian deltas and Hudson Bay lowlands, contributing to approximately 70% and 60% of emission increases in 2020 and 2021. Our findings underscore that wetland emissions dominate the interannual variability of methane sources and played key roles in the exceptionally high methane growth in 2020 and 2021. However, such strong emission increases from tropical inundated areas were substantially underestimated by current biogeochemical models, reflecting model deficiencies in representing year-to-year dynamics of tropical wetland extents and related methane emissions. This finding highlights the need for integrating multiple data streams and modeling tools to better constrain tropical wetland emissions and to understand their environmental sensitivities.

Methods

We followed the methodologies described in Peng et al. (2022) to combine both top-down and bottom-up approaches for a synthesis study of recent methane growth during 2020–2021. The analyses of methane emission changes were extended to 2021 on the basis of Peng et al. (2022) using similar data sources and modeling tools. We further included satellite-based CH_4 observations and flux inversions in addition to the analyses derived from surface CH_4 networks, which allows for intercomparison of the emission change patterns that are informed by different datasets of atmospheric CH_4 observations.

Atmospheric observations

For surface CH_4 observations, in-situ continuous and flask-air CH_4 measurements from a total of 121 stations for the inversion analyses were included (Supplementary Fig. 2), most of which are operated and maintained by the NOAA (Lan et al., 2022) and ICOS networks. Observations from other networks were obtained from the World Data Centre for Greenhouse Gases (https://gaw.kishou.go.jp) and the Global Environmental Database (https://db.cger.nies.go.jp). All observations are reported on or linked to the WMOX2004 calibration scale.

For satellite CH_4 observations, we used two retrievals of GOSAT XCH_4 provided by National Institute for Environmental Studies in Japan and the University of Leicester in the UK (denoted as "GSNIES" and "GSUoL" respectively). Launched by the Japan Aerospace Exploration Agency (JAXA) in early 2009, GOSAT achieves a global coverage every 3 days with a swath of 750 km and a ground pixel with a diameter of approximately 10.5 km at nadir. The Thermal And Near-infrared Sensor for Carbon Observation – Fourier Transform Spectrometer (TANSO-FTS) onboard enables the measurements of column-averaged dry-air CO_2 and CH_4 mole fractions by solar backscatter in the shortwave infrared (SWIR) with near-unit sensitivity across the air column down to the surface (Butz et al., 2011; Kuze et al., 2009). The two GOSAT XCH_4 products used here differ in their algorithms to treat the scattering-induced issues in the retrieval of total column concentrations from spectral data. The GSNIES XCH_4 retrieval was produced using a full-physics algorithm to infer CH_4 column together with physical scattering properties of the atmosphere (Yoshida et al., 2011, 2013). Alternatively, the GSUoL XCH_4 retrieval employed a proxy algorithm that simultaneously retrieves CH_4 and CO_2 columns using the absorption features around the wavelength of 1.6 μm to minimize the scattering effect on the retrieval (Parker et al., 2011, 2015). While the two conceptually different approaches have their own advantages and disadvantages (Schepers et al., 2012), the proxy retrieval is less sensitive to aerosol distribution and instrumental issues than the full-physics retrieval, therefore has much higher data density over geographic regions with substantial aerosol loading, such as in the tropics (Supplementary Fig. 3). In this study, we used the GSNIES XCH_4 retrieval version 2.95/2.96 (Inoue et al., 2016) and the GSUoL XCH_4 retrieval version 9.0 (Parker et al., 2020), which are bias-corrected and in good agreement with ground-based XCH_4 measurements from the Total Column Carbon Observing Network (TCCON) and aircraft-based CH_4 profile measurements. These two retrievals have been widely used in global or regional methane inverse modeling to study recent trends and interannual variabilities (Feng et al., 2023; Qu et al., 2022; Wang et al., 2021; Wilson et al., 2021; Yin et al., 2020). Note that only retrievals over land were assimilated in our inversions in order to avoid potential retrieval biases between nadir and glint viewing modes.

To calculate the atmospheric CH_4 growth rate, for surface observations, we used zonally averaged marine boundary layer (MBL) references for CH_4 constructed by NOAA's Global Monitoring Laboratory (NOAA/GML) using measurements of weekly air samples from a subset of sites in the NOAA Cooperative Global Air Sampling Network (Dlugokencky et al., 2021). Only sites that measure background atmospheric compositions are considered, typically at remote marine sea level locations with prevailing onshore winds. For GOSAT XCH_4 observations, we used daily means of all valid land retrievals per 10° latitude band for subsequent growth rate calculation. The smoothed CH_4 growth rate for each latitude band shown in Fig. 1 and Supplementary Fig. 1 was extracted from time series of the zonally-averaged MBL CH_4 references or GOSAT XCH_4 observations over the period 2010–2021 following the curve fitting procedures of Thoning et al. (1989).

Atmospheric 3D inversion

We used a variational Bayesian inversion system PYVAR-LMDZ-SACS to optimize weekly CH_4 surface fluxes at a spatial resolution of 1.9° in latitude by 3.75° in longitude over the period 2019–2021. An ensemble of six inversions was performed (Supplementary Table 1), each using a combination of three different observation datasets described above for constraints and two physical parameterizations for the transport model Laboratoire de Météorologie Dynamique with zooming capability (LMDZ), the atmospheric component of the coupled IPSL climate model participating in IPCC Assessment Reports (AR). These setups allowed us to explore consistency of the emission change patterns informed by different observation datasets while accounting for some of the uncertainties in atmospheric transport. The two physical parameterizations, denoted here as the "classic" and "standard" versions, represent two development stages of LMDZ for IPCC AR3 and AR6 (Hourdin et al., 2006, 2013, 2020). The "classic" AR3 version uses the vertical diffusion scheme of Louis (1979) to represent the turbulent transport in the boundary layer and the scheme of Tiedtke (1989) to parameterize deep convection (Hourdin et al., 2006). The "standard" AR6 version combines the vertical diffusion scheme of Mellor & Yamada (1974) and the thermal plume model by Rio & Hourdin (2008) to simulate the atmospheric mixing in the boundary layer, and the deep convection is represented using the scheme of Emanuel (1991) coupled with the parameterization of cold pools developed by Grandpeix et al. (2010) (Hourdin et al., 2013, 2020). While the "standard" version showed overall improved representation of boundary layer mixing and large-scale atmospheric transport (Locatelli et al., 2015a; Remaud et al., 2018, 2023), which would benefit trace gas transport simulations and inversions despite its comparatively larger computational costs, the "classic" version or its physical parameterization schemes are still widely used in the scientific community for methane studies (see Supplementary Table S6 in Saunois et al., 2020). A previous study by Locatelli et al. (2015b) showed that changing physical parameterizations would have small impact on the inverted methane emissions at the global scale (around 1%), but could lead to significant differences in the north–south gradient of emissions and the emission partitioning between regions.

Depending on the observations assimilated and the physical parameterizations used in the inversion system, discrepancies in the derived emission changes do exist among inversions at global or regional scales. The emission growth inferred from surface observations was much lower than those from GOSAT-based inversions for 2020 (Supplementary Fig. 5a), possibly because surface networks have limited spatial coverage over certain key source regions (e.g., the tropics), thus being blind to the methane growth there (Supplementary Fig. 2). Among the four GOSAT-based inversions, the ones constrained by GSUoL retrievals always gave 15–30% higher global net emission increases than those constrained by GSNIES retrievals (Supplementary Fig. 5a, b), consistent with the steeper rise of the methane growth rate seen from GSUoL (Fig. 1; Supplementary Fig. 1). For several important emitting regions such as eastern China, northern India and southern Africa, the directions of emission changes disagreed among inversions assimilating different observations (Supplementary Figs. 6 & 7), reflecting uncertainties in flux solution related to sparse data density or GOSAT XCH_4 retrieval algorithms.

Other configurations of the inversions followed the descriptions in Peng et al., (2022). The prior CH_4 fluxes were built on bottom-up inventories or process-based land surface models for different categories (Supplementary Table 5). The OH and $O(^1D)$ fields were prescribed from the simulation of a chemistry-climate model LMDZ-INCA with a full tropospheric photochemistry scheme (Hauglustaine et al., 2004, 2014). The model was run at the resolution of 1.27° in latitude by 2.5° in longitude, driven by interannually varying horizontal winds from ECMWF ERA5 reanalysis (Hersbach et al., 2018) and with natural and anthropogenic emissions of NO_x, CO and hydrocarbons updated to 2021 (Carbon Monitor; Community Emissions Data System (CEDS); van der Werf et al., 2017). The resulting oxidant fields were not adjusted in the inversions in order to keep the simulated OH changes from LMDZ-INCA. The preprocessing of surface CH_4 observations and the assignment of observation uncertainty were based on the protocol described in Peng et al. (2022). For GOSAT XCH_4 observations, the valid data were averaged into model grids for each time step (30 mins) to create "super-observations", with the observation errors defined as the retrieval errors reported by the data product plus model errors whose standard deviations were empirically set as 1% (Cressot et al., 2014; Yin et al., 2021).

Bottom-up estimates of methane emissions

Anthropogenic methane emissions were compiled from a combination of existing inventories. For the 42 Annex-I countries that report their national greenhouse gas inventories (NGHGIs) to UNFCCC each year, we used the reported anthropogenic methane emissions updated to 2021 from coal mining, oil and gas production, agriculture and waste sectors, respectively (https://unfccc.int/ghg-inventories-annex-i-parties/2023#fn2). For China, anthropogenic methane emissions were computed and updated to 2021 based on the activity data collected from national statistic books (National Bureau of Statistics of China, 2022) and specific emission factors at provincial levels (Liu et al., 2021; Peng et al., 2016). For other countries, emissions from coal mining, oil and gas production, agriculture and waste were obtained from the Emissions Database for Global Atmospheric Research version 7.0 (EDGAR v7.0; Crippa et al., 2021, 2022), with coal production and livestock data corrected by the activity data from International Energy Agency (IEA) and Food and Agriculture Organization of the United Nations (FAO). The national total emissions from the 42 Annex-I countries, China and other countries were distributed on $0.1° \times 0.1°$ grid cells based on the spatial patterns of EDGAR v7.0. Note that the change in global anthropogenic methane emissions between 2020 and 2019 slightly differs from that reported by Peng et al. (2022), as different versions of EDGAR and IEA data were used in this study to estimate emissions.

The global fire methane emissions were obtained from the Global Fire Emissions Database version 4.1 including small fire burned area (Randerson et al., 2012; van der Werf et al., 2017). The data set produces monthly gridded burned area and fire emissions at a spatial resolution of 0.25° × 0.25°, based on satellite information on fire activity and vegetation productivity (van der Werf et al., 2017).

For wetland emissions, we used two process-based wetland emission models (WEMs), ORCHIDEE-MICT (Guimberteau et al., 2018) and LPJ-wsl (Zhang et al., 2017), to simulate the global wetland CH_4 emissions. Based on the simulation protocol in Peng et al. (2022), wetland methane emissions were updated to 2021 using these two WEMs with four climate forcing datasets. The spatiotemporal dynamics of wetland areas were simulated by a TOPMODEL-based diagnostic model and applied to ORCHIDEE-MICT (Xi et al., 2021, 2022) and LPJ-wsl (Zhang et al., 2016), respectively. For ORCHIDEE-MICT in particular, we utilized two wetland maps to calibrate the parameters in simulating the wetland area dynamics (Xi et al., 2022). The static map of Regularly Flooded Wetlands (RFW; Tootchi et al., 2019) was applied for the grid-based calibration of the long-term maximum wetland extent, whereas the Global Inundation Estimate from Multiple Satellites version 2 (GIEMS-2; Prigent et al., 2020b) was applied to calibrate the yearly maximum wetland extent for each grid. Together, eight ORCHIDEE-MICT simulations and four LPJ-wsl simulations of wetland CH_4 emissions were included in our analyses.

References

Bloom, A. A., Palmer, P. I., Fraser, A., Reay, D. S., & Frankenberg, C. (2010). Large-Scale Controls of Methanogenesis Inferred from Methane and Gravity Spaceborne Data. *Science*, *327*(5963), 322–325. https://doi.org/10.1126/science.1175176

Butz, A., Guerlet, S., Hasekamp, O., Schepers, D., Galli, A., Aben, I., et al. (2011). Toward accurate CO2 and CH4 observations from GOSAT. *Geophysical Research Letters*, *38*(14). https://doi.org/10.1029/2011GL047888

Carbon Monitor. (2022). Retrieved May 1, 2022, from https://carbonmonitor.org/

Community Emissions Data System (CEDS). CEDS v_2021_04_21 gridded emissions data. (2021). Retrieved July 1, 2021, from https://data.pnnl.gov/dataset/CEDS-4-21-21

Cressot, C., Chevallier, F., Bousquet, P., Crevoisier, C., Dlugokencky, E. J., Fortems-Cheiney, A., et al. (2014). On the consistency between global and regional methane emissions inferred from SCIAMACHY, TANSO-FTS, IASI and surface measurements. *Atmospheric Chemistry and Physics*, *14*(2), 577–592. https://doi.org/10.5194/acp-14-577-2014

Crippa, M., Guizzardi, D., Solazzo, E., Muntean, M., Schaaf, E., Monforti-Ferrario, F., et al. (2021). *GHG emissions of all world countries - 2021 Report* (No. ISBN 978-92-76-41547-3). Publications Office of the European Union, Luxembourg. Retrieved from doi:10.2760/173513

Crippa, M., Guizzardi, D., Banja, M., Solazzo, E., Muntean, M., Schaaf, E., et al. (2022). *CO2 emissions of all world countries – JRC/IEA/PBL 2022 Report*. Publications Office of the European Union, Luxembourg. Retrieved from doi:10.2760/730164

Davis, S. J., Liu, Z., Deng, Z., Zhu, B., Ke, P., Sun, T., et al. (2022). Emissions rebound from the COVID-19 pandemic. *Nature Climate Change*, *12*(5), 412–414. https://doi.org/10.1038/s41558-022-01332-6

Delwiche, K. B., Knox, S. H., Malhotra, A., Fluet-Chouinard, E., McNicol, G., Feron, S., et al. (2021). FLUXNET-CH_4: a global, multi-ecosystem dataset and analysis of methane seasonality from freshwater wetlands. *Earth System Science Data*, *13*(7), 3607–3689. https://doi.org/10.5194/essd-13-3607-2021

Dlugokencky, E. J., Lan, X., Crotwell, A. M., Thoning, K. W., & Crotwell, M. J. (2021). Atmospheric Methane Dry Air Mole Fractions from the NOAA ESRL Carbon Cycle

Cooperative Global Air Sampling Network. Retrieved from ftp://aftp.cmdl.noaa.gov/data/trace_gases/ch4/flask/surface/

Emanuel, K. A. (1991). A Scheme for Representing Cumulus Convection in Large-Scale Models. *Journal of the Atmospheric Sciences*, *48*(21), 2313–2329. https://doi.org/10.1175/1520-0469(1991)048<2313:ASFRCC>2.0.CO;2

Feng, L., Palmer, P. I., Parker, R. J., Lunt, M. F., & Bösch, H. (2023). Methane emissions are predominantly responsible for record-breaking atmospheric methane growth rates in 2020 and 2021. *Atmospheric Chemistry and Physics*, *23*(8), 4863–4880. https://doi.org/10.5194/acp-23-4863-2023

Food and Agriculture Organization of the United Nations (FAO). (n.d.). FAOSTAT Emissions Land Use Database [Data set]. Retrieved from https://www.fao.org/faostat/en/#data

Gerlein-Safdi, C., Bloom, A. A., Plant, G., Kort, E. A., & Ruf, C. S. (2021). Improving Representation of Tropical Wetland Methane Emissions With CYGNSS Inundation Maps. *Global Biogeochemical Cycles*, *35*(12), e2020GB006890. https://doi.org/10.1029/2020GB006890

Grandpeix, J.-Y., Lafore, J.-P., & Cheruy, F. (2010). A Density Current Parameterization Coupled with Emanuel's Convection Scheme. Part II: 1D Simulations. *Journal of the Atmospheric Sciences*, *67*(4), 898–922. https://doi.org/10.1175/2009JAS3045.1

Guimberteau, M., Zhu, D., Maignan, F., Huang, Y., Yue, C., Dantec-Nédélec, S., et al. (2018). ORCHIDEE-MICT (v8.4.1), a land surface model for the high latitudes: model description and validation. *Geoscientific Model Development*, *11*(1), 121–163. https://doi.org/10.5194/gmd-11-121-2018

Hauglustaine, D. A., Hourdin, F., Jourdain, L., Filiberti, M.-A., Walters, S., Lamarque, J.-F., & Holland, E. A. (2004). Interactive chemistry in the Laboratoire de Météorologie Dynamique general circulation model: Description and background tropospheric chemistry evaluation. *Journal of Geophysical Research: Atmospheres*, *109*(D4). https://doi.org/10.1029/2003JD003957

Hauglustaine, D. A., Balkanski, Y., & Schulz, M. (2014). A global model simulation of present and future nitrate aerosols and their direct radiative forcing of climate. *Atmospheric Chemistry and Physics*, *14*(20), 11031–11063. https://doi.org/10.5194/acp-14-11031-2014

Helfter, C., Gondwe, M., Murray-Hudson, M., Makati, A., Lunt, M. F., Palmer, P. I., & Skiba, U. (2022). Phenology is the dominant control of methane emissions in a tropical non-forested wetland. *Nature Communications*, *13*(1), 133. https://doi.org/10.1038/s41467-021-27786-4

Hersbach, H., Bell, B., Berrisford, P., Biavati, G., Horányi, A., Muñoz Sabater, J., et al. (2018). ERA5 hourly data on single levels from 1959 to present. Copernicus Climate Change Service (C3S) Climate Data Store (CDS). (Accessed 1 March 2022). https://doi.org/10.24381/cds.adbb2d47

Hodson, E. L., Poulter, B., Zimmermann, N. E., Prigent, C., & Kaplan, J. O. (2011). The El Niño–Southern Oscillation and wetland methane interannual variability. *Geophysical Research Letters*, *38*(8). https://doi.org/10.1029/2011GL046861

Hourdin, F., Musat, I., Bony, S., Braconnot, P., Codron, F., Dufresne, J.-L., et al. (2006). The LMDZ4 general circulation model: climate performance and sensitivity to parametrized physics with emphasis on tropical convection. *Climate Dynamics*, *27*(7), 787–813. https://doi.org/10.1007/s00382-006-0158-0

Hourdin, F., Grandpeix, J.-Y., Rio, C., Bony, S., Jam, A., Cheruy, F., et al. (2013). LMDZ5B: the atmospheric component of the IPSL climate model with revisited parameterizations for clouds and convection. *Climate Dynamics*, *40*(9), 2193–2222. https://doi.org/10.1007/s00382-012-1343-y

Hourdin, F., Rio, C., Grandpeix, J., Madeleine, J., Cheruy, F., Rochetin, N., et al. (2020). LMDZ6A: The Atmospheric Component of the IPSL Climate Model With Improved and Better Tuned Physics. *Journal of Advances in Modeling Earth Systems*, *12*(7). https://doi.org/10.1029/2019MS001892

Inoue, M., Morino, I., Uchino, O., Nakatsuru, T., Yoshida, Y., Yokota, T., et al. (2016). Bias corrections of GOSAT SWIR XCO_2 and XCH_4 with TCCON data and their evaluation using aircraft measurement data. *Atmospheric Measurement Techniques*, *9*(8), 3491–3512. https://doi.org/10.5194/amt-9-3491-2016

International Energy Agency. (n.d.). World Energy Balances Highlights [Data set]. Retrieved from https://www.iea.org/data-and-statistics/data-product/world-energy-balances-highlights

Jackson, R. B., Friedlingstein, P., Quéré, C. L., Abernethy, S., Andrew, R. M., Canadell, J. G., et al. (2022). Global fossil carbon emissions rebound near pre-COVID-19 levels.

Environmental Research Letters, *17*(3), 031001. https://doi.org/10.1088/1748-9326/ac55b6

Kuze, A., Suto, H., Nakajima, M., & Hamazaki, T. (2009). Thermal and near infrared sensor for carbon observation Fourier-transform spectrometer on the Greenhouse Gases Observing Satellite for greenhouse gases monitoring. *Applied Optics*, *48*(35), 6716–6733. https://doi.org/10.1364/AO.48.006716

Lan, X., Dlugokencky, E. J., Mund, J. W., Crotwell, A. M., Crotwell, M. J., Moglia, E., et al. (2022). Atmospheric Methane Dry Air Mole Fractions from the NOAA GML Carbon Cycle Cooperative Global Air Sampling Network, 1983-2021 (Version 2022-11-21) [Data set]. https://doi.org/10.15138/VNCZ-M766

Lan, X., Thoning, K. W., & Dlugokencky, E. J. (2023). Trends in globally-averaged CH4, N2O, and SF6 determined from NOAA Global Monitoring Laboratory measurements. Version 2023-03. Retrieved from https://doi.org/10.15138/P8XG-AA10

Laughner, J. L., Neu, J. L., Schimel, D., Wennberg, P. O., Barsanti, K., Bowman, K. W., et al. (2021). Societal shifts due to COVID-19 reveal large-scale complexities and feedbacks between atmospheric chemistry and climate change. *Proceedings of the National Academy of Sciences*, *118*(46), e2109481118. https://doi.org/10.1073/pnas.2109481118

Li, X., Hu, Z.-Z., Tseng, Y., Liu, Y., & Liang, P. (2022). A Historical Perspective of the La Niña Event in 2020/2021. *Journal of Geophysical Research: Atmospheres*, *127*(7), e2021JD035546. https://doi.org/10.1029/2021JD035546

Liu, G., Peng, S., Lin, X., Ciais, P., Li, X., Xi, Y., et al. (2021). Recent Slowdown of Anthropogenic Methane Emissions in China Driven by Stabilized Coal Production. *Environmental Science & Technology Letters*. https://doi.org/10.1021/acs.estlett.1c00463

Locatelli, R., Bousquet, P., Hourdin, F., Saunois, M., Cozic, A., Couvreux, F., et al. (2015a). Atmospheric transport and chemistry of trace gases in LMDz5B: evaluation and implications for inverse modelling. *Geoscientific Model Development*, *8*(2), 129–150. https://doi.org/10.5194/gmd-8-129-2015

Locatelli, R., Bousquet, P., Saunois, M., Chevallier, F., & Cressot, C. (2015b). Sensitivity of the recent methane budget to LMDz sub-grid-scale physical parameterizations. *Atmospheric Chemistry and Physics*, *15*(17), 9765–9780. https://doi.org/10.5194/acp-15-9765-2015

Louis, J.-F. (1979). A parametric model of vertical eddy fluxes in the atmosphere. *Boundary-Layer Meteorology*, *17*(2), 187–202. https://doi.org/10.1007/BF00117978

Lunt, M. F., Palmer, P. I., Feng, L., Taylor, C. M., Boesch, H., & Parker, R. J. (2019). An increase in methane emissions from tropical Africa between 2010 and 2016 inferred from satellite data. *Atmospheric Chemistry and Physics*, *19*(23), 14721–14740. https://doi.org/10.5194/acp-19-14721-2019

Lunt, M. F., Palmer, P. I., Lorente, A., Borsdorff, T., Landgraf, J., Parker, R. J., & Boesch, H. (2021). Rain-fed pulses of methane from East Africa during 2018–2019 contributed to atmospheric growth rate. *Environmental Research Letters*, *16*(2), 024021. https://doi.org/10.1088/1748-9326/abd8fa

Mellor, G. L., & Yamada, T. (1974). A Hierarchy of Turbulence Closure Models for Planetary Boundary Layers. *Journal of the Atmospheric Sciences*, *31*(7), 1791–1806. https://doi.org/10.1175/1520-0469(1974)031<1791:AHOTCM>2.0.CO;2

Miyazaki, K., Bowman, K., Sekiya, T., Takigawa, M., Neu, J. L., Sudo, K., et al. (2021). Global tropospheric ozone responses to reduced NOx emissions linked to the COVID-19 worldwide lockdowns. *Science Advances*, *7*(24), eabf7460. https://doi.org/10.1126/sciadv.abf7460

National Bureau of Statistics of China. (2022). *China Statistical Yearbook*. Retrieved from http://www.stats.gov.cn/english/statisticaldata/annualdata

Pandey, S., Houweling, S., Krol, M., Aben, I., Monteil, G., Nechita-Banda, N., et al. (2017). Enhanced methane emissions from tropical wetlands during the 2011 La Niña. *Scientific Reports*, *7*(1), 1–8. https://doi.org/10.1038/srep45759

Pandey, S., Houweling, S., Lorente, A., Borsdorff, T., Tsivlidou, M., Bloom, A. A., et al. (2021). Using satellite data to identify the methane emission controls of South Sudan's wetlands. *Biogeosciences*, *18*(2), 557–572. https://doi.org/10.5194/bg-18-557-2021

Pangala, S. R., Enrich-Prast, A., Basso, L. S., Peixoto, R. B., Bastviken, D., Hornibrook, E. R. C., et al. (2017). Large emissions from floodplain trees close the Amazon methane budget. *Nature*, *552*(7684), 230–234. https://doi.org/10.1038/nature24639

Parker, R., Boesch, H., Cogan, A., Fraser, A., Feng, L., Palmer, P. I., et al. (2011). Methane observations from the Greenhouse Gases Observing SATellite: Comparison to ground-based TCCON data and model calculations. *Geophysical Research Letters*, *38*(15). https://doi.org/10.1029/2011GL047871

Parker, R. J., Boesch, H., Byckling, K., Webb, A. J., Palmer, P. I., Feng, L., et al. (2015). Assessing 5 years of GOSAT Proxy XCH_4 data and associated uncertainties. *Atmospheric Measurement Techniques*, *8*(11), 4785–4801. https://doi.org/10.5194/amt-8-4785-2015

Parker, R. J., Boesch, H., McNorton, J., Comyn-Platt, E., Gloor, M., Wilson, C., et al. (2018). Evaluating year-to-year anomalies in tropical wetland methane emissions using satellite CH_4 observations. *Remote Sensing of Environment*, *211*, 261–275. https://doi.org/10.1016/j.rse.2018.02.011

Parker, R. J., Webb, A., Boesch, H., Somkuti, P., Barrio Guillo, R., Di Noia, A., et al. (2020). A decade of GOSAT Proxy satellite CH_4 observations. *Earth System Science Data*, *12*(4), 3383–3412. https://doi.org/10.5194/essd-12-3383-2020

Parker, R. J., Wilson, C., Comyn-Platt, E., Hayman, G., Marthews, T. R., Bloom, A. A., et al. (2022). Evaluation of wetland CH_4 in the Joint UK Land Environment Simulator (JULES) land surface model using satellite observations. *Biogeosciences*, *19*(24), 5779–5805. https://doi.org/10.5194/bg-19-5779-2022

Peng, S., Piao, S., Bousquet, P., Ciais, P., Li, B., Lin, X., et al. (2016). Inventory of anthropogenic methane emissions in mainland China from 1980 to 2010. *Atmospheric Chemistry and Physics*, *16*(22), 14545–14562. https://doi.org/10.5194/acp-16-14545-2016

Peng, S., Lin, X., Thompson, R. L., Xi, Y., Liu, G., Hauglustaine, D., et al. (2022). Wetland emission and atmospheric sink changes explain methane growth in 2020. *Nature*, *612*(7940), 477–482. https://doi.org/10.1038/s41586-022-05447-w

Prigent, C., Jimenez, C., & Bousquet, P. (2020). Satellite-Derived Global Surface Water Extent and Dynamics Over the Last 25 Years (GIEMS-2). *Journal of Geophysical Research: Atmospheres*, *125*(3), e2019JD030711. https://doi.org/10.1029/2019JD030711

Qu, Z., Jacob, D. J., Zhang, Y., Shen, L., Varon, D. J., Lu, X., et al. (2022). Attribution of the 2020 surge in atmospheric methane by inverse analysis of GOSAT observations. *Environmental Research Letters*, *17*(9), 094003. https://doi.org/10.1088/1748-9326/ac8754

Randerson, J. T., Chen, Y., van der Werf, G. R., Rogers, B. M., & Morton, D. C. (2012). Global burned area and biomass burning emissions from small fires. *Journal of Geophysical Research: Biogeosciences*, *117*(G4). https://doi.org/10.1029/2012JG002128

Remaud, M., Chevallier, F., Cozic, A., Lin, X., & Bousquet, P. (2018). On the impact of recent developments of the LMDz atmospheric general circulation model on the simulation of CO_2 transport. *Geoscientific Model Development*, *11*(11), 4489–4513. https://doi.org/10.5194/gmd-11-4489-2018

Remaud, M., Ma, J., Krol, M., Abadie, C., Cartwright, M. P., Patra, P., et al. (2023). Intercomparison of Atmospheric Carbonyl Sulfide (TransCom-COS; Part One): Evaluating the Impact of Transport and Emissions on Tropospheric Variability Using Ground-Based and Aircraft Data. *Journal of Geophysical Research: Atmospheres*, *128*(6), e2022JD037817. https://doi.org/10.1029/2022JD037817

Rio, C., & Hourdin, F. (2008). A Thermal Plume Model for the Convective Boundary Layer: Representation of Cumulus Clouds. *Journal of the Atmospheric Sciences*, *65*(2), 407–425. https://doi.org/10.1175/2007JAS2256.1

Saunois, M., Stavert, A. R., Poulter, B., Bousquet, P., Canadell, J. G., Jackson, R. B., et al. (2020). The Global Methane Budget 2000–2017. *Earth System Science Data*, *12*(3), 1561–1623. https://doi.org/10.5194/essd-12-1561-2020

Schepers, D., Guerlet, S., Butz, A., Landgraf, J., Frankenberg, C., Hasekamp, O., et al. (2012). Methane retrievals from Greenhouse Gases Observing Satellite (GOSAT) shortwave infrared measurements: Performance comparison of proxy and physics retrieval algorithms. *Journal of Geophysical Research: Atmospheres*, *117*(D10). https://doi.org/10.1029/2012JD017549

Shaw, J. T., Allen, G., Barker, P., Pitt, J. R., Pasternak, D., Bauguitte, S. J.-B., et al. (2022). Large Methane Emission Fluxes Observed From Tropical Wetlands in Zambia. *Global Biogeochemical Cycles*, *36*(6), e2021GB007261. https://doi.org/10.1029/2021GB007261

Thoning, K. W., Tans, P. P., & Komhyr, W. D. (1989). Atmospheric carbon dioxide at Mauna Loa Observatory: 2. Analysis of the NOAA GMCC data, 1974–1985. *Journal of Geophysical Research: Atmospheres*, *94*(D6), 8549–8565. https://doi.org/10.1029/JD094iD06p08549

Tiedtke, M. (1989). A Comprehensive Mass Flux Scheme for Cumulus Parameterization in Large-Scale Models. *Monthly Weather Review*, *117*(8), 1779–1800. https://doi.org/10.1175/1520-0493(1989)117<1779:ACMFSF>2.0.CO;2

Tootchi, A., Jost, A., & Ducharne, A. (2019). Multi-source global wetland maps combining surface water imagery and groundwater constraints. *Earth System Science Data*, *11*(1), 189–220. https://doi.org/10.5194/essd-11-189-2019

Wang, F., Maksyutov, S., Janardanan, R., Tsuruta, A., Ito, A., Morino, I., et al. (2021). Interannual variability on methane emissions in monsoon Asia derived from GOSAT and surface observations. *Environmental Research Letters*, *16*(2), 024040. https://doi.org/10.1088/1748-9326/abd352

van der Werf, G. R., Randerson, J. T., Giglio, L., van Leeuwen, T. T., Chen, Y., Rogers, B. M., et al. (2017). Global fire emissions estimates during 1997–2016. *Earth System Science Data*, *9*(2), 697–720. https://doi.org/10.5194/essd-9-697-2017

Wilson, C., Chipperfield, M. P., Gloor, M., Parker, R. J., Boesch, H., McNorton, J., et al. (2021). Large and increasing methane emissions from eastern Amazonia derived from satellite data, 2010–2018. *Atmospheric Chemistry and Physics*, *21*(13), 10643–10669. https://doi.org/10.5194/acp-21-10643-2021

Xi, Y., Peng, S., Ciais, P., & Chen, Y. (2021). Future impacts of climate change on inland Ramsar wetlands. *Nature Climate Change*, *11*(1), 45–51. https://doi.org/10.1038/s41558-020-00942-2

Xi, Y., Peng, S., Ducharne, A., Ciais, P., Gumbricht, T., Jimenez, C., et al. (2022). Gridded maps of wetlands dynamics over mid-low latitudes for 1980–2020 based on TOPMODEL. *Scientific Data*, *9*(1), 347. https://doi.org/10.1038/s41597-022-01460-w

Yin, Y., Chevallier, F., Ciais, P., Bousquet, P., Saunois, M., Zheng, B., et al. (2020). Accelerating methane growth rate from 2010 to 2017: leading contributions from the tropics and East Asia. *Atmospheric Chemistry and Physics Discussions*, 1–27. https://doi.org/10.5194/acp-2020-649

Yin, Y., Chevallier, F., Ciais, P., Bousquet, P., Saunois, M., Zheng, B., et al. (2021). Accelerating methane growth rate from 2010 to 2017: leading contributions from the tropics and East Asia. *Atmos. Chem. Phys.*, 17.

Yoshida, Y., Ota, Y., Eguchi, N., Kikuchi, N., Nobuta, K., Tran, H., et al. (2011). Retrieval algorithm for CO_2 and CH_4 column abundances from short-wavelength infrared spectral observations by the Greenhouse gases observing satellite. *Atmospheric Measurement Techniques*, *4*(4), 717–734. https://doi.org/10.5194/amt-4-717-2011

Yoshida, Y., Kikuchi, N., Morino, I., Uchino, O., Oshchepkov, S., Bril, A., et al. (2013). Improvement of the retrieval algorithm for GOSAT SWIR XCO_2 and XCH_4 and their validation using TCCON data. *Atmospheric Measurement Techniques*, *6*(6), 1533–1547. https://doi.org/10.5194/amt-6-1533-2013

Zhang, Z., Zimmermann, N. E., Kaplan, J. O., & Poulter, B. (2016). Modeling spatiotemporal dynamics of global wetlands: comprehensive evaluation of a new sub-grid TOPMODEL parameterization and uncertainties. *Biogeosciences*, *13*(5), 1387–1408. https://doi.org/10.5194/bg-13-1387-2016

Zhang, Z., Zimmermann, N. E., Stenke, A., Li, X., Hodson, E. L., Zhu, G., et al. (2017). Emerging role of wetland methane emissions in driving 21st century climate change. *Proceedings of the National Academy of Sciences*, *114*(36), 9647–9652. https://doi.org/10.1073/pnas.1618765114

Zhang, Z., Poulter, B., Feldman, A. F., Ying, Q., Ciais, P., Peng, S., & Li, X. (2023). Recent intensification of wetland methane feedback. *Nature Climate Change*, 1–4. https://doi.org/10.1038/s41558-023-01629-0

Zheng, B., Chevallier, F., Yin, Y., Ciais, P., Fortems-Cheiney, A., Deeter, M. N., et al. (2019). Global atmospheric carbon monoxide budget 2000–2017 inferred from multi-species atmospheric inversions. *Earth System Science Data*, *11*(3), 1411–1436. https://doi.org/10.5194/essd-11-1411-2019

Zheng, B., Ciais, P., Chevallier, F., Yang, H., Canadell, J. G., Chen, Y., et al. (2023). Record-high CO2 emissions from boreal fires in 2021. *Science*, *379*(6635), 912–917. https://doi.org/10.1126/science.ade0805

Zhu, Q., Peng, C., Ciais, P., Jiang, H., Liu, J., Bousquet, P., et al. (2017). Interannual variation in methane emissions from tropical wetlands triggered by repeated El Niño Southern Oscillation. *Global Change Biology*, *23*(11), 4706–4716. https://doi.org/10.1111/gcb.13726

Data availability

The datasets that support the findings of this study are publicly available as follows. The global atmospheric methane growth rates and marine boundary layer references are obtained from https://gml.noaa.gov/ccgg/trends_ch4 and https://gml.noaa.gov/ccgg/mbl/ respectively. The assimilated surface CH_4 observations from NOAA and ICOS networks are available at https://doi.org/10.15138/VNCZ-M766 and https://doi.org/10.18160/KCYX-HA35; surface observations from other networks are available from World Data Centre for Greenhouse Gases (https://gaw.kishou.go.jp/) and Global Environmental Database (https://db.cger.nies.go.jp/). The GOSAT NIES full physics XCH_4 retrievals are available at https://data2.gosat.nies.go.jp/ through registration; the GOSAT University of Leicester proxy XCH_4 retrievals are available at https://catalogue.ceda.ac.uk/uuid/18ef8247f52a4cb6a14013f8235cc1eb. The EDGAR v7.0 time series of country-level emissions and sector-specific gridmaps are downloaded from https://edgar.jrc.ec.europa.eu/dataset_ghg70. The hourly ERA5 reanalysis data are obtained from https://www.ecmwf.int/en/forecasts/dataset/ecmwf-reanalysis-v5. The monthly dataset of temperature and precipitation from CRU TS v4.06 are obtained from https://crudata.uea.ac.uk/cru/data/hrg/cru_ts_4.06/. The monthly precipitation data from MERRA2 are obtained from https://gmao.gsfc.nasa.gov/reanalysis/MERRA-2/. The monthly precipitation from MSWEP v2.8 are obtained from http://www.gloh2o.org/mswep/. The dataset of monthly global water storage/height anomalies from GRACE-FO is available at https://doi.org/10.5067/TEMSC-3JC63. The Regular Flooded Wetlands maps are available at https://doi.pangaea.de/10.1594/PANGAEA.892657. The monthly fire emissions from Global Fire Emissions Database version 4.1, which includes small fire burned area, are obtained from https://www.geo.vu.nl/~gwerf/GFED/GFED4/. The anthropogenic emissions from the CEDS emission inventory up to 2019 are available at https://data.pnnl.gov/dataset/CEDS-4-21-21. The gridded near-real time fossil fuel combustion data that include confinement-induced reductions in 2020 and rebound in 2021 are obtained from https://carbonmonitor.org/.

Code availability

The codes and documentation for the process-based wetland models ORCHIDEE-MICT (v8.4.4) and LPJ-wsl are publicly available at http://forge.ipsl.jussieu.fr/orchidee/ and https://github.com/benpoulter/LPJ-wsl_v2.0.git, respectively. The global chemistry transport model LMDZ-INCA is part of the coupled IPSL climate model, with its codes and documentation available at https://cmc.ipsl.fr/ipsl-climate-models/ipsl-cm6/.

Acknowledgements

The study was funded by the ESA CCI RECCAP2 project (ESRIN/4000123002/18/I-NB). P.C. also acknowledges the support from the ANR CLAND convergence institute. R.J.P. and H.B. were funded via the UK National Centre for Earth Observation (grant nos. NE/R016518/1 and NE/N018079/1), as well as from the ESA GHG-CCI and Copernicus C3S projects (grant no. C3S2_312a_Lot2). We are very grateful to the scientists and technicians who are running surface networks of CH_4 observations and make these datasets available. We thank the Japanese Aerospace Exploration Agency, National Institute for Environmental Studies and the Ministry of Environment for the GOSAT data and their continuous support as part of the Joint Research Agreement. This research is supported through HPC resources of TGCC under the allocation A0110102201 made by GENCI for LMDZ-INCA simulations and computing mass fluxes, the Peking University supercomputing facility for ORCHIDEE-MICT simulations, and the ALICE high-performance computing facility at the University of Leicester for the GOSAT retrievals and analysis. We also acknowledge the technical support from the IT team of LSCE.

Author contributions

X. Lin, S.P. and P.C. designed the study. X. Lin performed atmospheric 3D inversions, with precomputed mass fluxes prepared by M. Remaud. G.L. and S.P. built the bottom-up anthropogenic emissions inventory. S.P. and Y.X. performed ORCHIDEE simulations; Z.Z. and B.P. performed LPJ-wsl simulations. D.H. and B.Z. performed LMDZ-INCA simulations. M. Ramonet and X. Lan provided surface CH_4 observations; Y. Yoshida provided GOSAT NIES full physics XCH_4 retrievals; R.J.P. and H.B. provided GOSAT University of Leicester proxy XCH_4 retrievals. C.G.-S. and T.P. provided CYGNSS inundation maps. X. Lin coordinated the research and conducted the analyses; S.H. and D.B. help preprocess the data. X. Lin drafted the first manuscript; S.P., P.C., X. Lan, Y. Yin, Z.Z., H.B., P.B., F.C., C.G.-S., R.J.P, B.P., M. Remaud, A.R., M.S., R.L.T., Y. Yoshida and B.Z. contributed to writing and commenting on the draft manuscript.

Competing interests

The authors declare no competing interests.

Additional information

Correspondence should be addressed to Xin Lin (xin.lin@lsce.ipsl.fr).

Figure 1. Variations of atmospheric methane growth rates between 2010 and 2021. a–d, Methane growth rates were derived from zonally averaged observations of NOAA Global Monitor Laboratory (NOAA/GML) marine boundary layer (MBL) sites (Lan et al., 2023), GOSAT NIES retrievals (Inoue et al., 2016) or GOSAT UoL retrievals (Parker et al., 2020), following the curve-fitting routines of Thoning et al. (1989). For **c**, **d**, results are not shown north of 50°N or south of 50°S due to data gaps of GOSAT retrievals over these regions during winter.

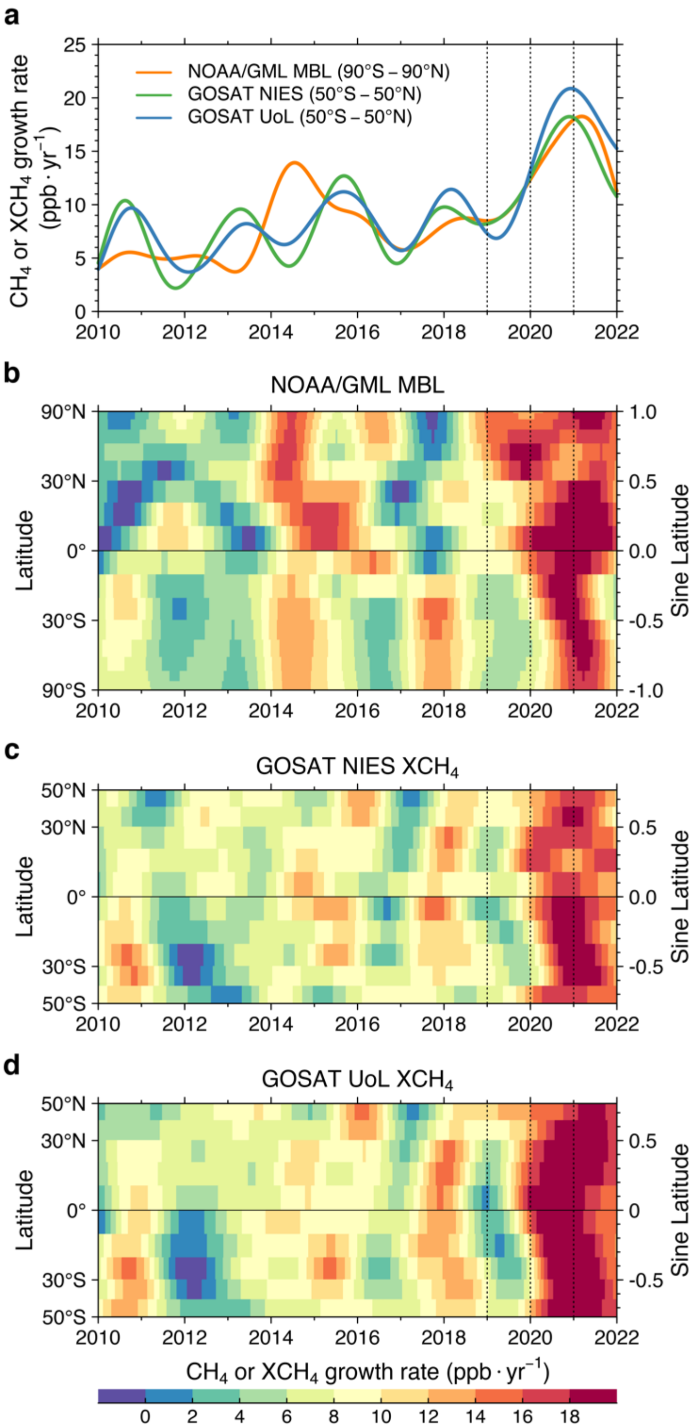

Figure 2. Methane emission anomalies in 2020 and 2021 relative to 2019 inferred from six inversions in relation to changes in satellite observed liquid water equivalent (LWE). a, b, Spatial patterns of the mean CH_4 emission anomalies averaged over the six inversions of the ensemble. The shaded areas indicate that posterior fluxes from all six inversions have the same changing direction. The inset bar plots summarize the net emission changes at the global scale and for four latitude bands. Error bars represent one standard deviation of the six inversions. **c, d,** Spatial patterns of changes in LWE from the GRACE-FO satellites. **e, g,** Scatterplot of CH_4 emission anomalies versus changes in GRACE-FO LWE across 20 major wetland regions defined based on the regularly flooded wetland map (Tootchi et al., 2019) in **f**. Each circle represents a major wetland region, with the size scaling with the magnitude of the region's posterior methane emission in 2019 (unit: Tg CH_4 yr^{-1}). The color of the circle corresponds to the color code for each wetland region in **f**.

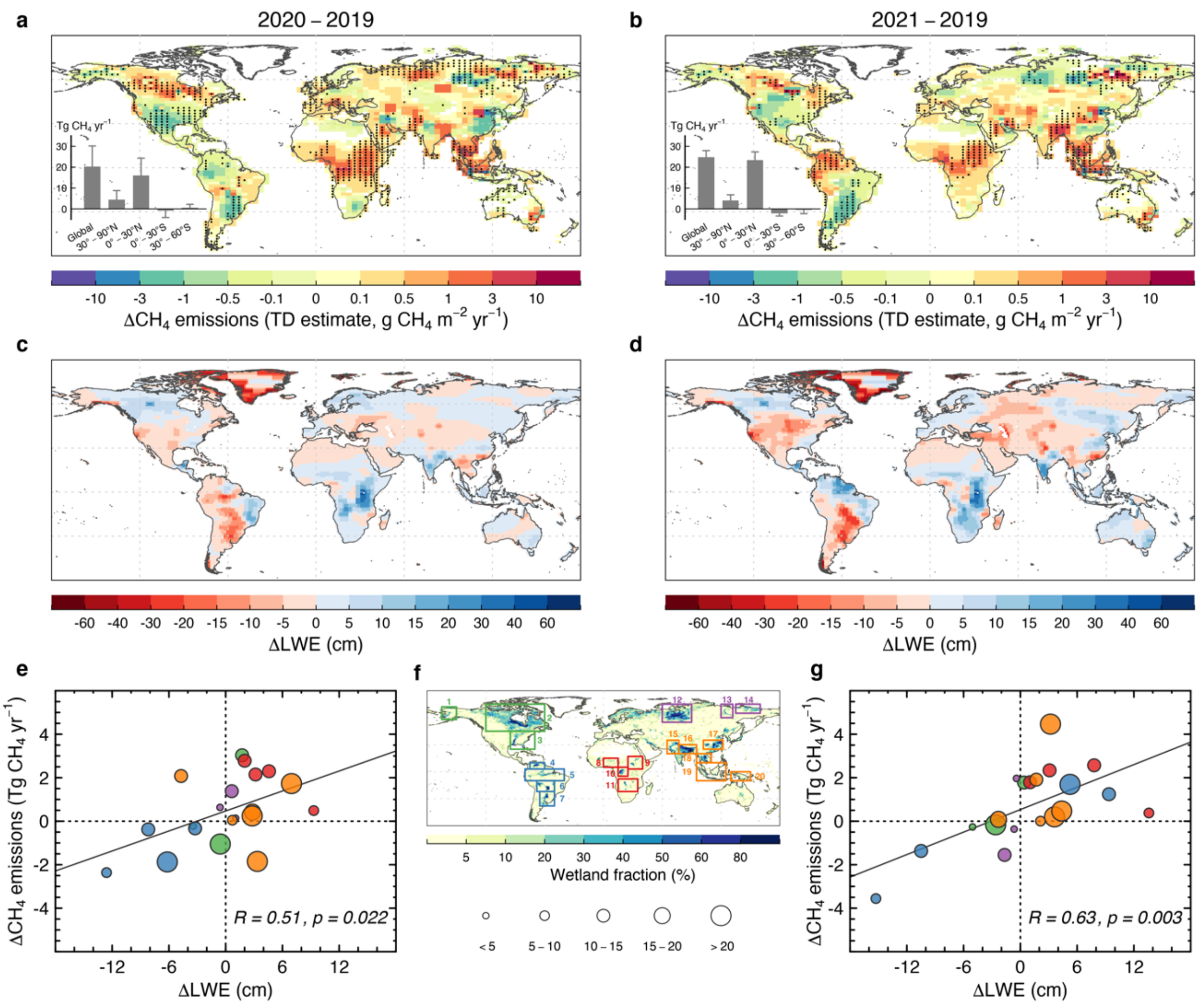

Figure 3. Top-down versus bottom-up estimates of methane emission anomalies in 2020 and 2021 relative to 2019. a, b, Mean methane emission anomalies of four latitude bands derived from the ensemble of six top-down inversions and bottom-up estimates. The black dots represent the net global emission changes relative to 2019. **c, d,** Spatial patterns of bottom-up CH_4 emission anomalies summed up from process-based wetland models, inventories of anthropogenic and fire emissions. The color scale is the same as for the top-down CH_4 emission anomalies in Fig. 2a, b. The inset bar plots summarize the net emission changes at the global scale and for four latitude bands. **e, f,** Top-down versus bottom-up estimates of methane emission anomalies for five tropical inundated areas. The delineation of each inundated area is shown in Fig. 2f and Supplementary Fig. 5g. The open circle indicates two times the interannual variability (2σ) of methane emissions during 2010–2019 derived from a previous study using the inversion system PYVAR-LMDZ-SACS and GSUoL as constraints for CH_4 (Zheng et al., 2019). Error bars in all panels denote one standard deviation of the methane emission anomalies from the ensemble of top-down or bottom-up estimates.

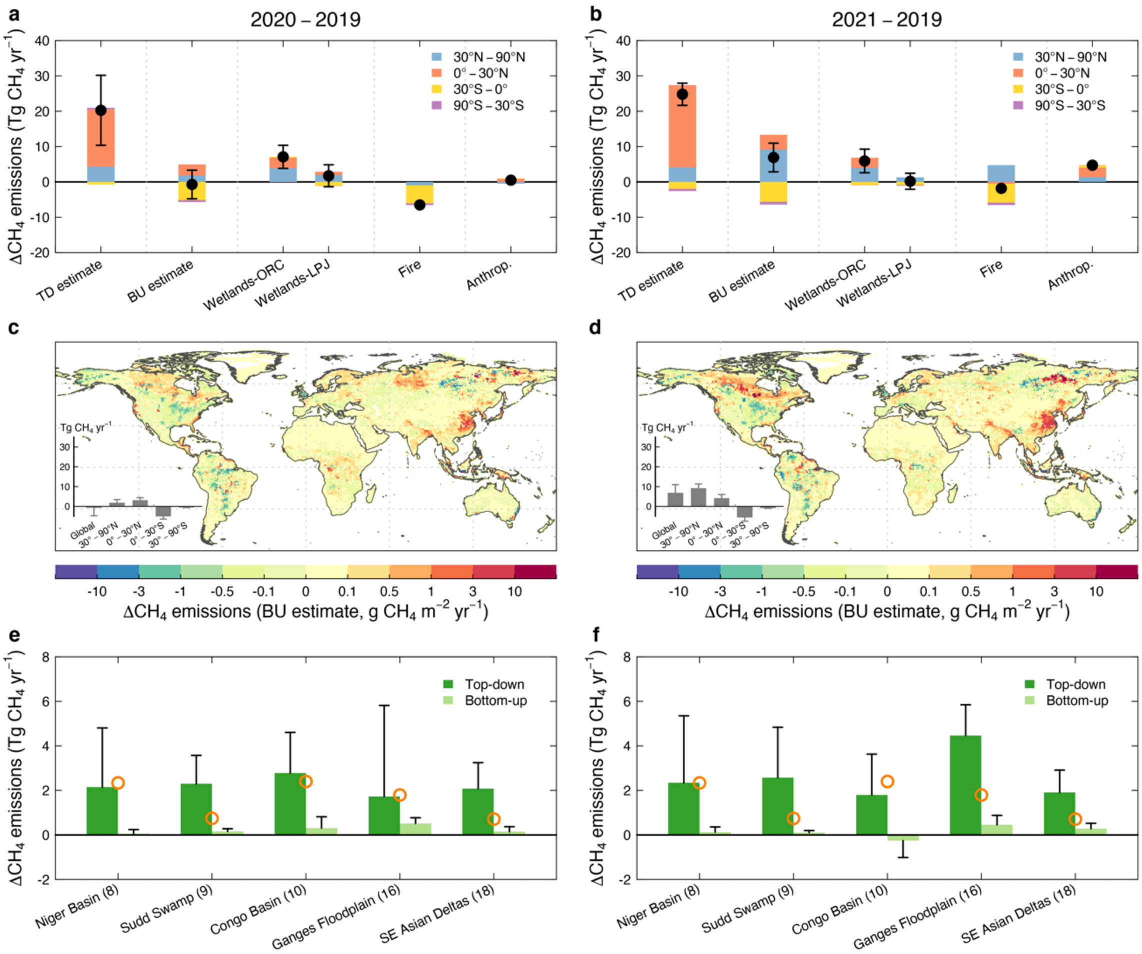

Supplementary Information for

Recent methane surges reveal heightened emissions from tropical inundated areas

X. Lin[1], S. Peng[2], P. Ciais[1,3] , D. Hauglustaine[1], X. Lan[4,5], G. Liu[2], M. Ramonet[1], Y. Xi[1,2], Y. Yin[6], Z. Zhang[7], H. Bösch[8,9], P. Bousquet[1], F. Chevallier[1], B. Dong[2], C. Gerlein-Safdi[10], S. Halder[1], R. J. Parker[8,9], B. Poulter[11], T. Pu[10], M. Remaud[1], A. Runge[12], M. Saunois[1], R. L. Thompson[13], Y. Yoshida[14], B. Zheng[15,16]

[1]Laboratoire des Sciences du Climat et de l'Environnement, LSCE/IPSL, CEA-CNRS-UVSQ, Université Paris-Saclay, Gif-sur-Yvette, France

[2]Sino-French Institute for Earth System Science, College of Urban and Environmental Sciences, Peking University, Beijing, China

[3]Climate and Atmosphere Research Center (CARE-C), The Cyprus Institute, Nicosia, Cyprus

[4]Cooperative Institute for Research in Environmental Sciences of University of Colorado, Boulder, CO, USA

[5]Global Monitoring Laboratory, National Oceanic and Atmospheric Administration, Boulder, CO, USA

[6]Division of Geological and Planetary Sciences, California Institute of Technology, Pasadena, CA, USA

[7]National Tibetan Plateau Data Centre, State Key Laboratory of Tibetan Plateau Earth System, Environment and Resource, Institute of Tibetan Plateau Research, Chinese Academy of Sciences, Beijing, China

[8]National Centre for Earth Observation, Space Park Leicester, University of Leicester, Leicester, UK

[9]Earth Observation Science, School of Physics and Astronomy, University of Leicester, Leicester, UK

[10]Department of Civil and Environmental Engineering, University of California, Berkeley, CA, USA

[11]Biospheric Sciences Laboratory, NASA Goddard Space Flight Center, Greenbelt, MD, USA

[12]Alfred Wegener Institute, Helmholtz Centre for Polar and Marine Research, Potsdam, Germany

[13]Norwegian Institute for Air Research (NILU), Kjeller, Norway

[14]National Institute for Environmental Studies, Tsukuba, Japan

[15]Institute of Environment and Ecology, Tsinghua Shenzhen International Graduate School, Tsinghua University, Shenzhen, China

[16]State Environmental Protection Key Laboratory of Sources and Control of Air Pollution Complex, Beijing, China

*Correspondence to Xin Lin (xin.lin@lsce.ipsl.fr)

Contents of this file

Supplementary Figure 1 | Variations of atmospheric methane growth rates between 2010 and 2021 at the global scale and for three latitude bands. **a–d,** Methane growth rates were derived from zonally averaged observations of NOAA Global Monitor Laboratory (NOAA/GML) marine boundary layer (MBL) sites (Lan et al., 2023), GOSAT NIES retrievals (Inoue et al., 2016) or GOSAT UoL retrievals (Parker et al., 2020), following the curve-fitting routines of Thoning et al. (1989).

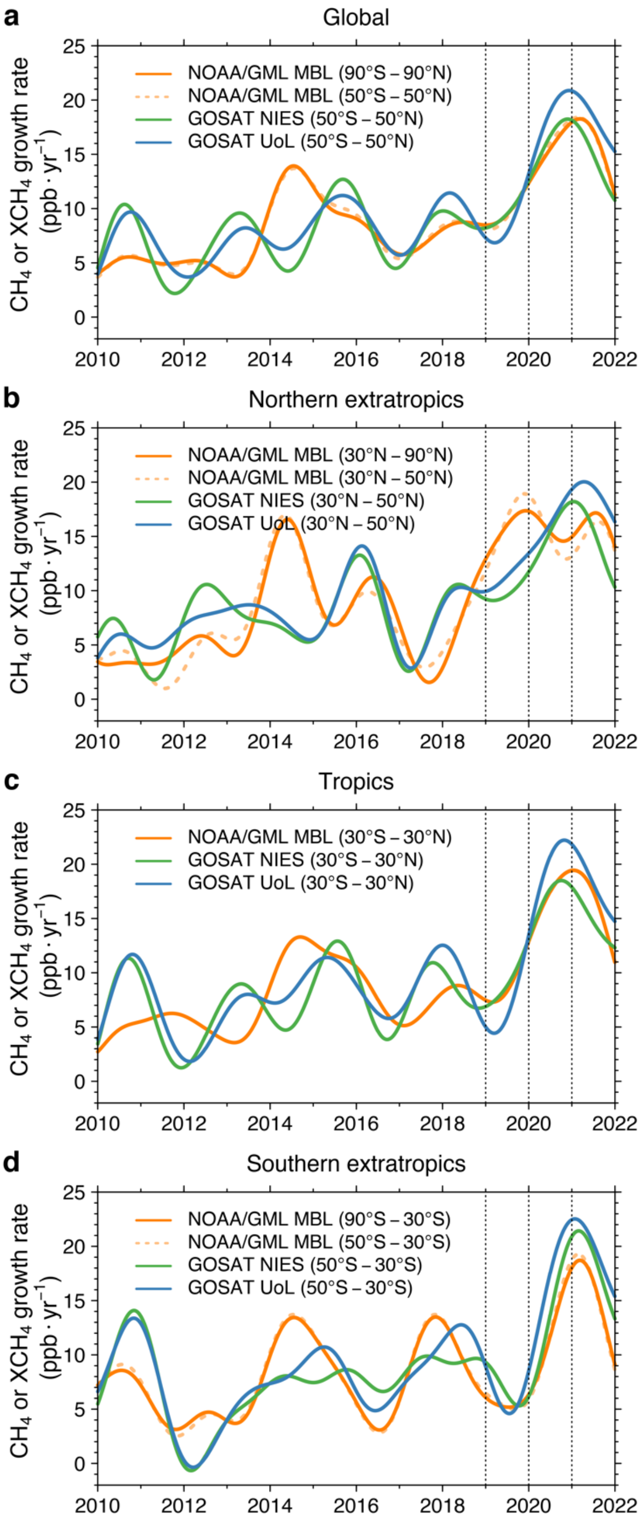

Supplementary Figure 2 | Map of surface stations for in-situ and flask-air CH_4 samplings used in the inversions. Blue circles represent stations with observations before 12/2021, while red crosses represent stations with observations extending to 12/2021 and afterwards.

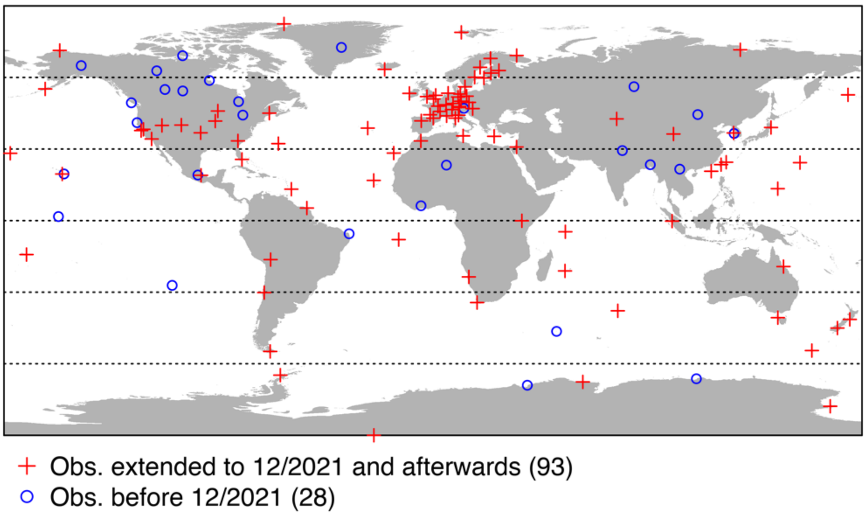

Supplementary Figure 3 | The number of XCH_4 observations for GOSAT University of Leicester (UoL) proxy retrievals and GOSAT NIES full physics retrievals. Each panel maps the number of XCH_4 "super-observations" (see Methods) on the model grids (1.9° in latitude by 3.75° in longitude) for a 3-month period of 2020.

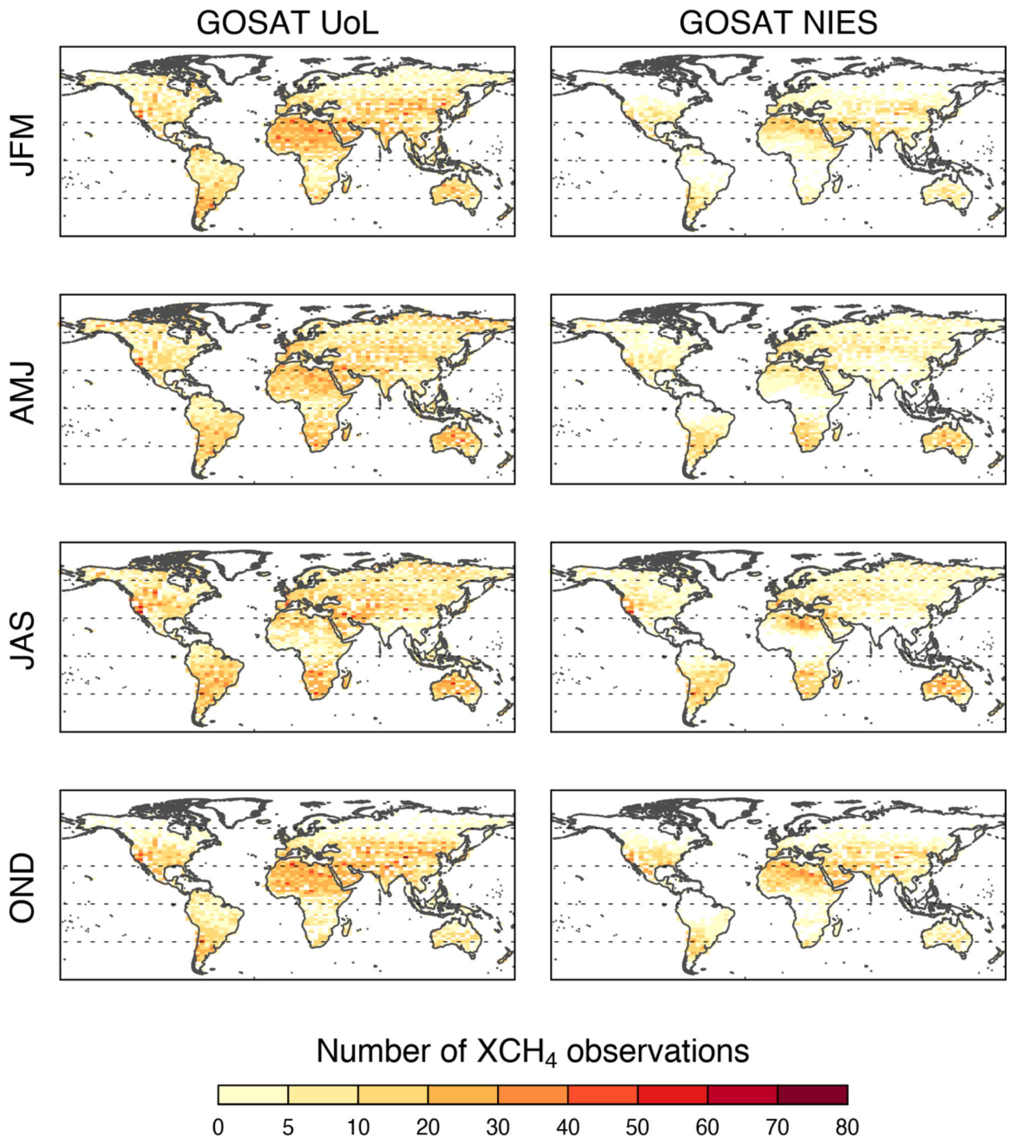

Supplementary Figure 4 | Anomalies of NO_x and CO emissions and tropospheric hydroxyl radical (OH) concentrations in 2020–2021 relative to 2019. **a-b, d-e, g-h,** Spatial patterns of emission anomalies of NO_x (ΔNO_x emissions) and CO (ΔCO emissions), and anomalies of tropospheric OH (ΔOH) in 2020–2021 relative to 2019. **c, f, i,** Changes in monthly global emissions of NO_x and CO and monthly tropospheric OH in 2020–2021 relative to 2019. The anthropogenic NO_x and CO emission data were obtained from the Community Emissions Data System (Community Emissions Data System (CEDS)) and Carbon Monitor (Carbon Monitor). The CO emissions from biomass burning were obtained from GFEDv4.1s (van der Werf et al., 2017). The OH concentration fields were simulated from a full chemistry transport model LMDZ-INCA (see the main text and Methods for details).

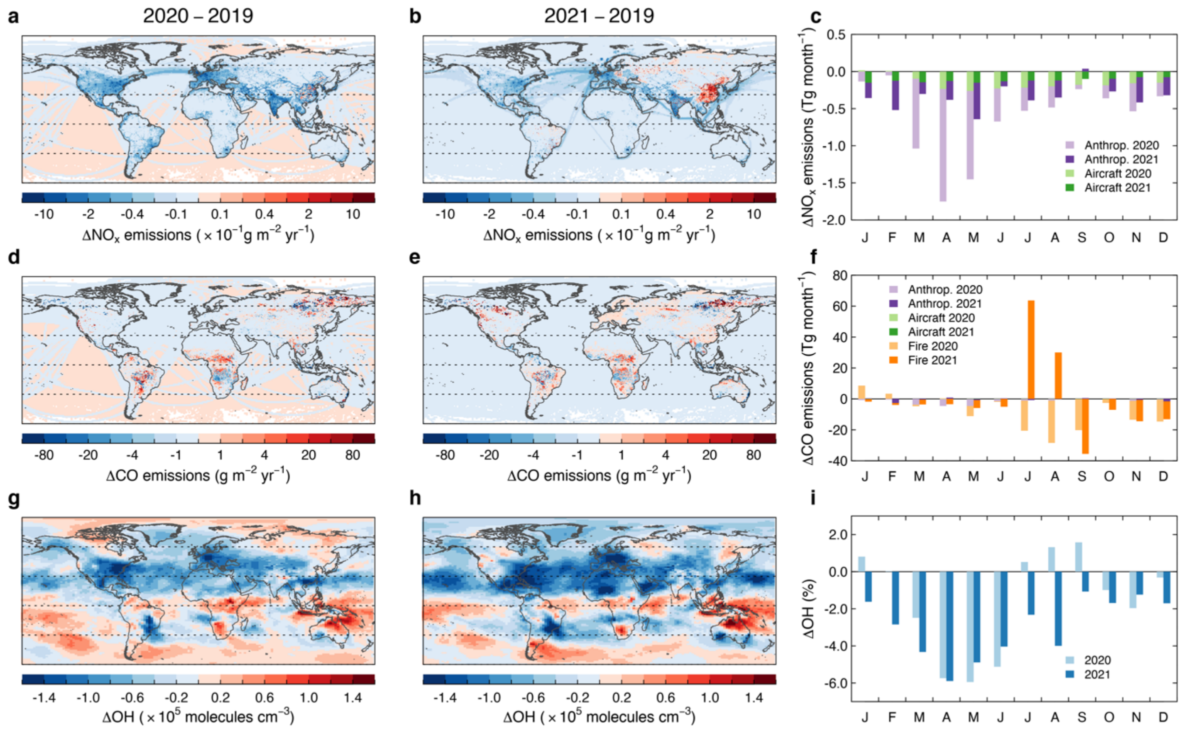

Supplementary Figure 5 | Methane emission anomalies in 2020 and 2021 relative to 2019 inferred from six inversions in relation to changes in GRACE-FO LWE. **a, b,** Methane emission anomalies of four latitude bands from six inversions. The black dots indicate the global net emission changes. The error bars represent one standard deviation. Refer to Supplementary Table 1 and Methods for descriptions and configurations of the inversion ensemble. **c, d,** Spatial patterns of CH_4 emission anomalies averaged over the six inversions. The shaded areas indicate that posterior fluxes from all six inversions have the same changing direction. **e, f,** Spatial patterns of changes in GRACE-FO LWE in 2020–2021 relative to 2019. **g,** Map of wetland fractions based on regularly flooded wetlands (Tootchi et al., 2019). Twenty major wetland regions were selected and marked in **c–f** to demonstrate emission anomalies over these regions in relation to changes in GRACE-FO LWE.

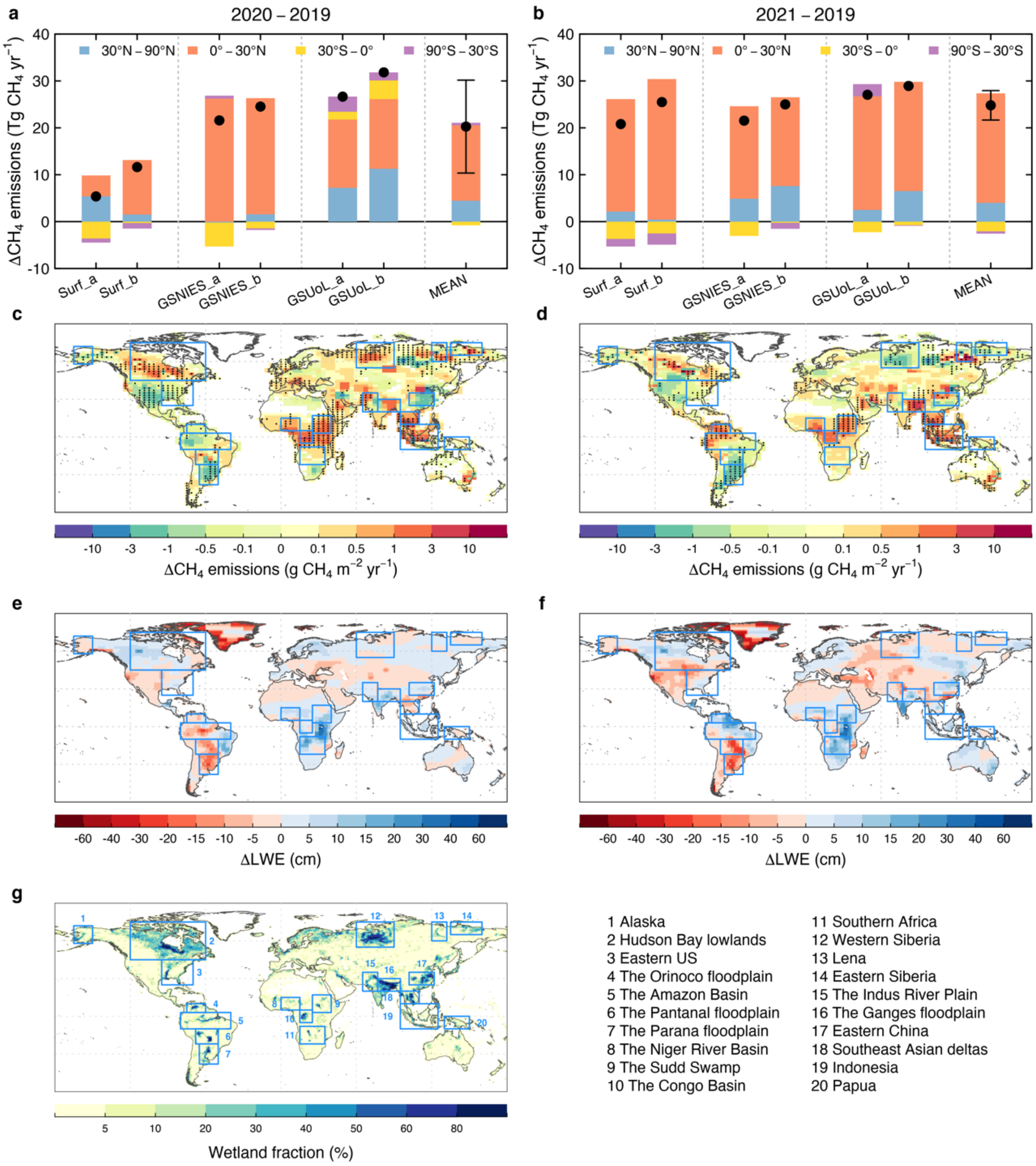

Supplementary Figure 6 | Anomalies of CH_4 emissions in 2020 relative to 2019 derived from the ensemble of six inversions. **a-f,** Spatial patterns of CH_4 emission anomalies derived from each member of the ensemble. The global net emission change (in unit Tg CH_4 yr^{-1}) is given for each panel on the bottom right. **g,** Spatial pattern of CH_4 emission anomalies averaged over the ensemble of six inversions. The shaded areas indicate that posterior fluxes from all six inversions have the same changing direction. **h,** Coefficient of variation in the CH_4 emission anomalies from the ensemble of six inversions. For each model grid, the coefficient of variation is defined as the standard deviation (SD) of emission anomalies from six inversions divided by the absolute value of their mean. Darker colors indicate better agreement among inversions. Refer to Supplementary Table 1 and Methods for detailed description and configurations of the inversion ensemble.

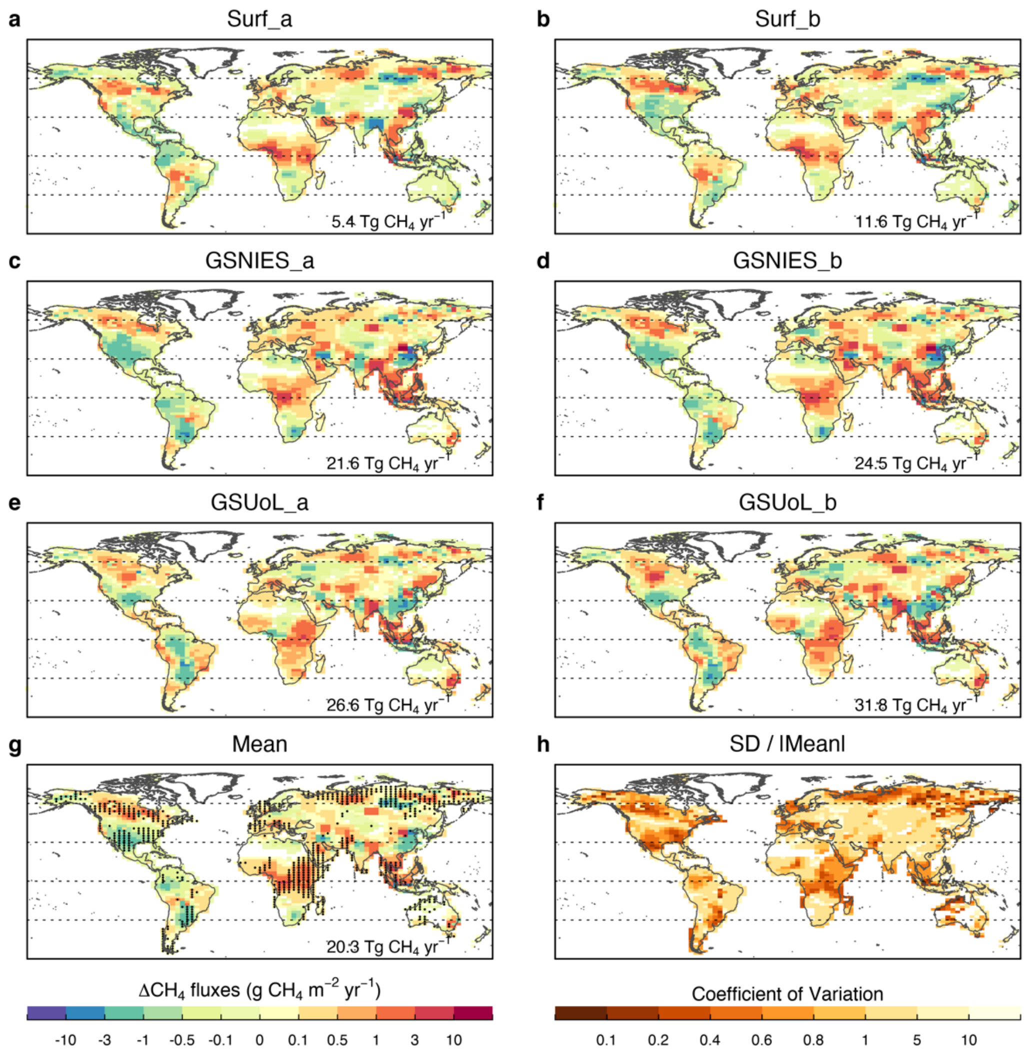

Supplementary Figure 7 | The same as Supplementary Figure 6, but for 2021.

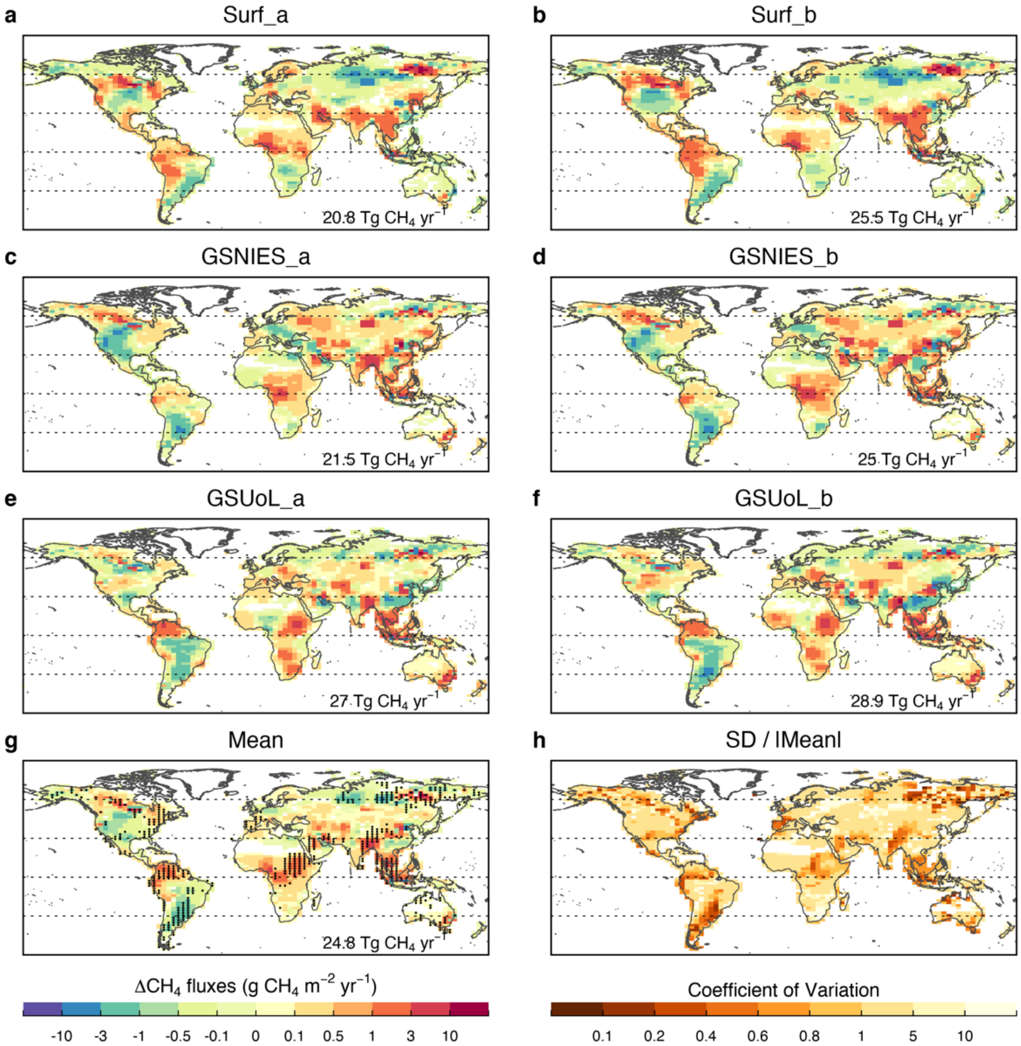

Supplementary Figure 8 | ** Top-down versus bottom-up estimates of methane emission anomalies in 2020 and 2021 relative to 2019. **a, b, Mean methane emission anomalies of four latitude bands derived from the ensemble of six top-down inversions and bottom-up estimates. The black dots represent the net global emission changes relative to 2019. **c–l,** Spatial patterns of top-down or bottom-up CH_4 emission anomalies. The inset bar plots summarize the net emission changes at the global scale and for four latitude bands.

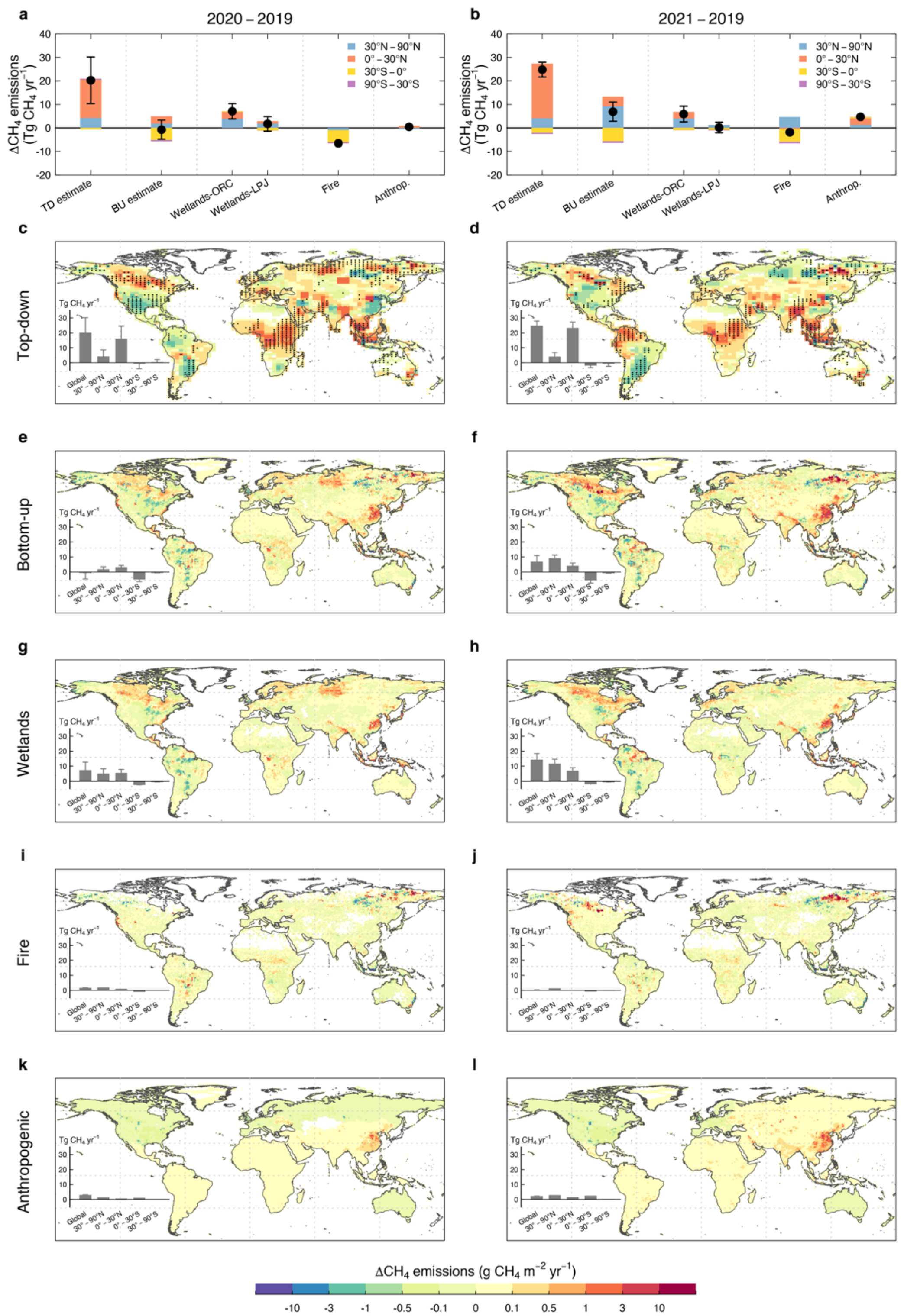

Supplementary Figure 9 | Wetland methane emission anomalies in 2020 and 2021 relative to 2019 simulated from two process-based wetland models ORCHIDEE-MICT and LPJ-wsl. **a, b,** Changes in wetland methane emissions were averaged for four latitude bands, based on simulations with four different climate forcing data (CRU, ERA5, MERRA2 and MSWEP). For ORCHIDEE-MICT, wetland area dynamics were calibrated by RFW and GIEMS2, respectively (noted as "ORCHIDEE-RFW" and "ORCHIDEE-GIEMS2"). The black dots represent the net changes of global wetland methane emissions.

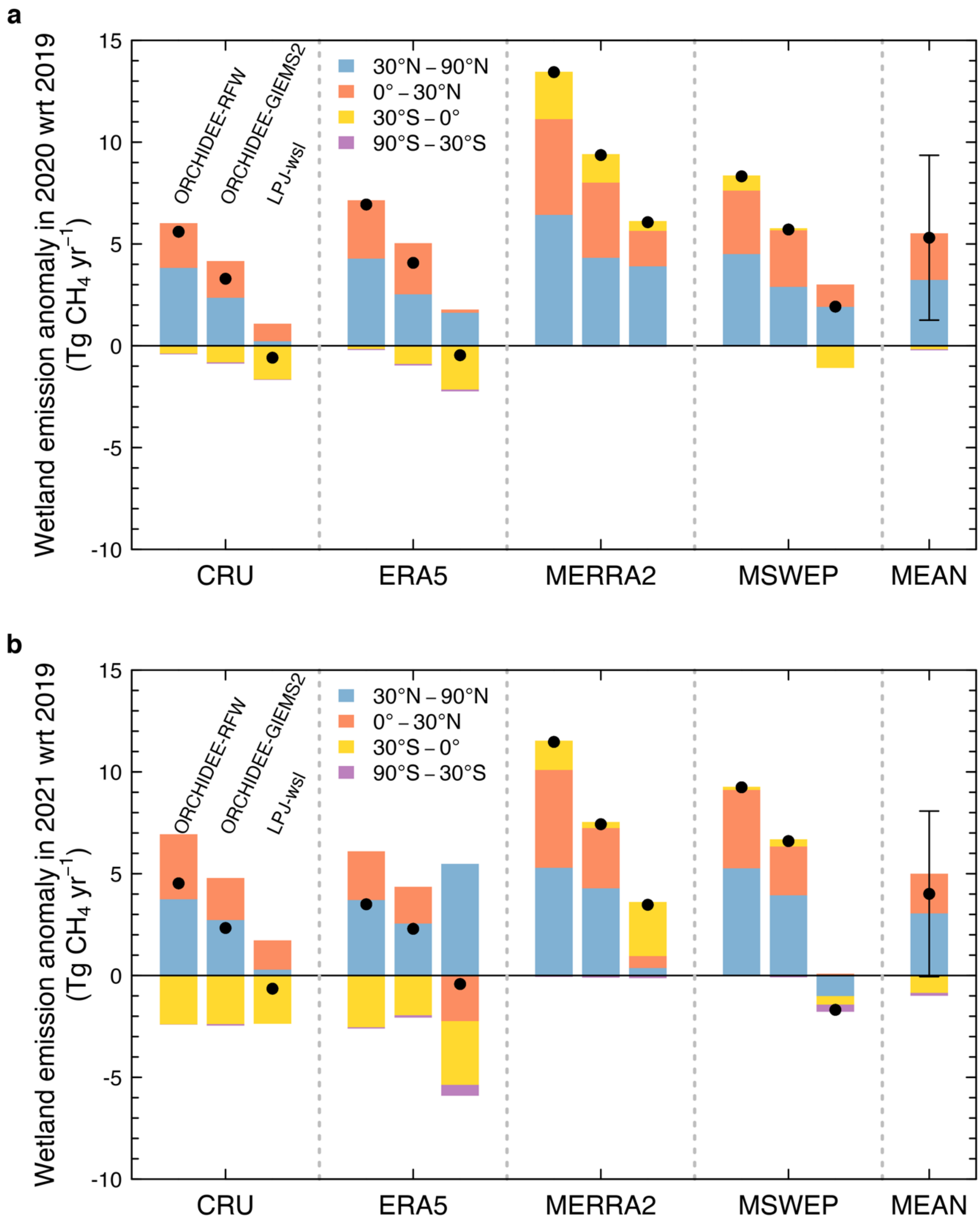

Supplementary Figure 10 | a, The seasonal variations in CH_4 emissions over the Sudd Swamp in the eastern Africa (3°N–17°N, 25°E–40°E) in relation to the seasonal changes in GRACE-FO LWE anomalies. **b,** Changes in monthly CH_4 emissions and GRACE-FO LWE anomalies between 2020–2021 and 2019. The black curves indicate the total CH_4 emissions (or emission changes relative to 2019) averaged across the ensemble of six inversions, with the grey shaded areas representing the ranges of estimates. Note that the total CH_4 emissions plotted here were the posterior CH_4 emissions with soil sinks from Murguia-Flores et al. (2018, 2021) excluded. The solid green curves indicate the mean wetland CH_4 emissions (or emission changes relative to 2019) averaged across the ensemble of wetland model simulations except LPJ-wsl driven by MERRA2 climate forcing, with the shaded areas representing the ranges of estimates. The dotted green curves show results from LPJ-wsl with MERRA2, which simulated larger seasonal variations of emissions, but failed to capture the emission enhancements during 2020–2021 as other simulations did. Refer to Supplementary Fig. 5g for the delineation of the region.

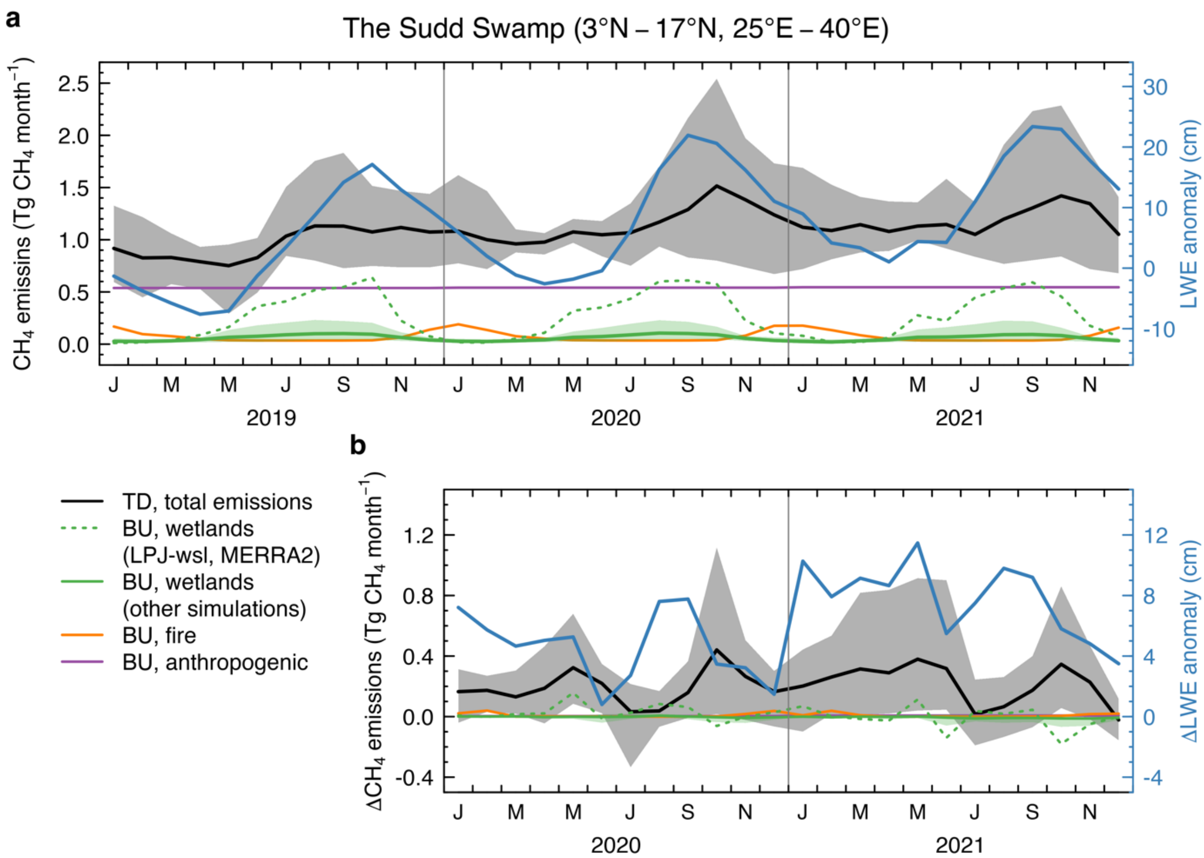

Supplementary Figure 11 | The monthly variations of simulated versus observed wetland extents for the Sudd Swamp in the eastern Africa (3°N–17°N, 25°E–40°E). The black line represents monthly observed wetland extents obtained from the inundation maps based on the Cyclone Global Navigation Satellite System (CYGNSS; Gerlein-Safdi et al., 2021; Gerlein-Safdi & Ruf, 2019). The colored lines represent simulated wetland dynamics by ORCHIDEE-MICT with four different climate forcing data (CRU, ERA5, MERRA2, MSWEP) and two wetland maps (GIEMS-2, RFW) for calibration of parameters (Xi et al., 2022).

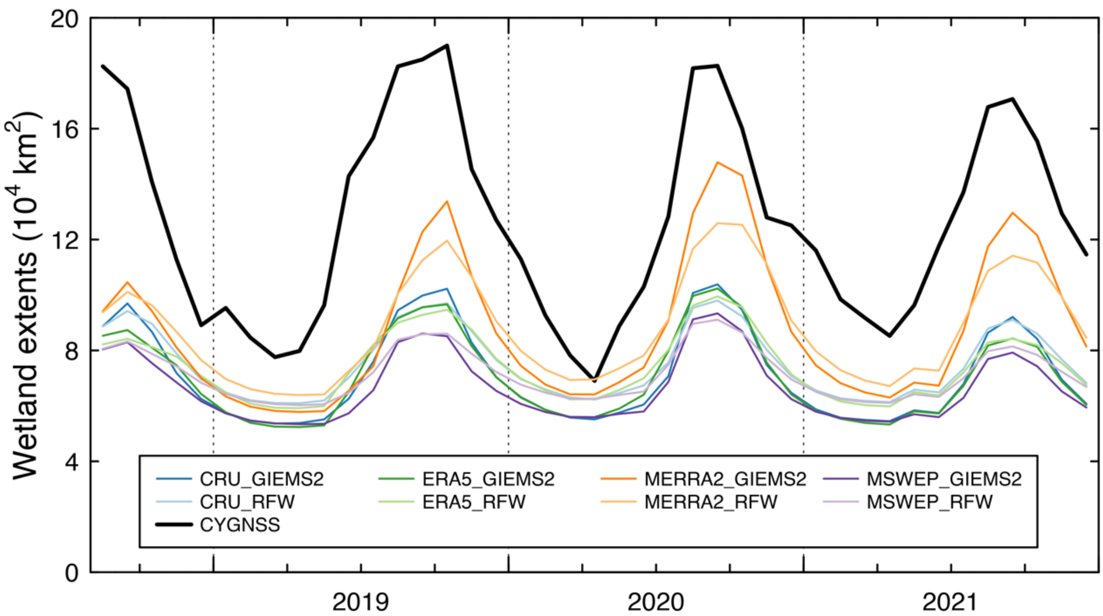

Supplementary Table 1 | Configurations of the ensemble of six inversions performed in this study (see Methods for more details).

Inversions	Observations assimilated	Physical parameterizations for transport
Surf_a	Surface networks	LMDZ “classic” AR3 version
Surf_b		LMDZ “standard” AR6 version
GSNIES_a	GOSAT XCH_4 NIES full physics retrievals	LMDZ “classic” AR3 version
GSNIES_b		LMDZ “standard” AR6 version
GSUoL_a	GOSAT XCH_4 Univ. Leicester proxy retrievals	LMDZ “classic” AR3 version
GSUoL_b		LMDZ “standard” AR6 version

Supplementary Table 2 | Changes in NO_x and CO emissions and tropospheric hydroxyl radical concentrations ($[OH]_{trop}$) in 2020 and 2021 relative to 2019. The numbers in the parentheses represent the percentages of changes in emissions with respect to the 2019 levels.

	2020 – 2019	2021 – 2019
NO_x	**–7.5 Tg yr^{-1} (–6.2%)**	**–4.2 Tg yr^{-1} (–3.5%)**
NO_x – Surface emissions	–5.7 Tg yr^{-1} (–4.8%)	–2.8 Tg yr^{-1} (–2.4%)
NO_x – Aviation emissions	–1.9 Tg yr^{-1} (–47.9%)	–1.4 Tg yr^{-1} (–36.0%)
CO	**–110.8 Tg yr^{-1} (–12.1%)**	**+1.3 Tg yr^{-1} (+0.15%)**
CO – Surface emissions	–19.0 Tg yr^{-1} (–3.6%)	–4.1 Tg yr^{-1} (–0.78%)
CO – Aviation emissions	–0.35 Tg yr^{-1} (–47.9%)	–0.26 Tg yr^{-1} (–36.0%)
CO – Fire emissions	–91.4 Tg yr^{-1} (–23.7%)	+5.7 Tg yr^{-1} (+1.5%)
$[OH]_{trop}$	**–1.5%**	**–3.0%**

Supplementary Table 3 | The bottom-up estimates versus top-down estimates of methane emission changes in 2020 (a) and 2021 (b) compared to 2019 at the global scale and over four latitudinal bands (unit: Tg CH_4 yr^{-1}). For comparison, the interannual variability (IAV) of emissions during 2010–2019 is derived from a previous study using the inversion system PYVAR-LMDZ-SACS and GSUoL as constraints for CH_4 (Zheng et al., 2019), calculated as one standard deviation of detrended emission anomalies.

(a)

	Global	30°N–90°N	0°–30°N	30°S–0°	90°S–30°S
BU	-0.7±4.0	1.8±1.6	3.2±1.3	-5.1±1.3	-0.6±0.0
Anthropogenic	0.5	-0.5	0.8	0.1	0.0
Fire	-6.5	-0.9	0.0	-5.1	-0.5
Wetland	5.3±4.0	3.2±1.6	2.3±1.3	-0.2±1.3	0.0±0.0
TD	20.3±9.9	4.3±4.3	16.2±8.3	-0.7±3.3	0.4±1.7
IAV of emissions (2010–2019)	6.7	4.6	3.6	5.3	0.4

(b)

	Global	30°N–90°N	0°–30°N	30°S–0°	90°S–30°S
BU	6.9±4.1	9.2±2.1	4.1±1.9	-5.6±1.9	-0.8±0.2
Anthropogenic	4.7	1.4	2.7	0.6	0.0
Fire	-1.8	4.7	-0.5	-5.4	-0.7
Wetland	4.0±4.1	3.1±2.1	1.9±1.9	-0.9±1.9	-0.1±0.2
TD	24.8±3.1	4.1±2.7	23.2±4.0	-2.0±1.3	-0.6±1.8
IAV of emissions (2010–2019)	6.7	4.6	3.6	5.3	0.4

Supplementary Table 4 | The bottom-up estimates versus top-down estimates of methane emission changes in 2020 and 2021 compared to 2019 over 20 major wetland regions (unit: Tg CH_4 yr^{-1}). For comparison, the interannual variability (IAV) of emissions during 2010–2019 is derived for each region from a previous study using the inversion system PYVAR-LMDZ-SACS and GSUoL as constraints for CH_4 (Zheng et al., 2019), calculated as one standard deviation of detrended emission anomalies. The delineation of the 20 major wetland regions is presented in Supplementary Fig. 5g. The lines in bold correspond to the five wetland regions plotted in Fig. 3e, f.

No.	Wetland regions	2020–2019		2021–2019		IAV of emissions (2010–2019)
		BU	TD	BU	TD	
1	Alaska	-0.4±0.2	-0.2±0.2	-0.3±0.1	-0.3±0.2	0.1
2	Hudson Bay lowlands	0.1±0.4	3.0±1.0	3.5±1.0	1.8±2.8	1.2
3	Eastern US	-0.6±0.3	-1.1±0.3	-0.8±0.4	-0.2±0.2	0.1
4	The Orinoco floodplain	-0.1±0.7	-0.3±0.3	0.0±1.2	1.2±1.3	0.4
5	The Amazon Basin	-1.5±0.6	-1.9±1.6	-0.6±0.8	1.7±2.7	1.6
6	The Pantanal floodplain	-0.1±0.4	-0.4±1.3	-0.8±0.7	-1.4±1.7	0.9
7	The Parana floodplain	-0.5±0.5	-2.4±1.3	-0.6±0.4	-3.6±1.4	0.5
8	**The Niger River Basin**	**0.1±0.2**	**2.1±2.7**	**0.1±0.2**	**2.3±3.0**	**1.2**
9	**The Sudd Swamp**	**0.2±0.1**	**2.3±1.3**	**0.1±0.1**	**2.6±2.3**	**0.4**
10	**The Congo Basin**	**0.3±0.5**	**2.8±1.8**	**-0.3±0.8**	**1.8±1.8**	**1.2**
11	Southern Africa	-0.1±0.2	0.5±1.3	0.0±0.1	0.4±1.7	0.3
12	Western Siberia	1.0±0.5	1.4±0.6	0.0±0.2	-1.6±2.7	0.8
13	Lena	0.0±0.0	0.1±0.3	1.7±0.0	2.0±2.0	0.1
14	Eastern Siberia	0.6±0.1	0.6±0.4	-0.1±0.1	-0.4±0.2	0.1
15	The Indus River Plain	0.2±0.2	0.4±0.9	0.4±0.3	0.1±0.8	0.2
16	**The Ganges floodplain**	**0.5±0.3**	**1.7±4.1**	**0.5±0.4**	**4.5±1.4**	**0.9**
17	Eastern China	2.0±0.6	-1.8±3.5	3.4±0.9	0.2±1.4	0.7
18	**Southeast Asian deltas**	**0.1±0.2**	**2.1±1.2**	**0.3±0.2**	**1.9±1.0**	**0.4**
19	Indonesia	-3.4±0.3	0.2±2.1	-3.4±0.5	0.5±2.1	2.3
20	Papua	0.5±0.4	0.0±0.4	0.6±0.6	0.0±0.4	0.2

Supplementary Table 5 | The prior CH_4 fluxes used in the inversions. All emission maps were regridded to 1.9° in latitude by 3.75° in longitude, the spatial resolution of the inversions.

Categories	Data sources	Temporal resolution	Original spatial resolution	Total flux for 2020 ($Tg\ CH_4\ yr^{-1}$)
Anthropogenic	EDGARv6.0 (Crippa et al., 2020). Data for the year 2019 were either scaled with FAO statistics (for the agricultural sector), or scaled with BP statistics (for coal, oil and gas production), or linearly propagated. Data for the year 2020 and 2021 were set equal to 2019. Emissions from agricultural waste burnings in EDGARv6.0 were excluded to avoid double counting with GFEDv4.1s.	Monthly, with IAV	0.1°	377.8
Biomass burning	GEFDv4.1s (van der Werf et al., 2017). Data from 2017 onward are beta data.	Monthly, with IAV	0.25°	12.9
Wetlands	Monthly climatological emissions averaged over 2008–2017 from 11 land surface models contributing to wetland emissions published in Saunois et al. (2020). TEM-MDM and ELM were excluded due to high negative fluxes.	Fixed, with seasonality	1°	151.1
Termites	Climatological emissions without seasonality from S. Castaldi's simulation (Saunois et al., 2020).	Fixed, without seasonality	1°	9.9
Ocean	Climatological emissions without seasonality from Weber et al. (2019).	Fixed, without seasonality	1°	11.5
Geological	Climatological emissions without seasonality from Etiope et al. (2019), rescaled to a global total of 23 Tg (best value given by IPCC AR6 WG1 report). Only onshore emissions were included to avoid double counting of offshore emissions with ocean emission sources.	Fixed, without seasonality	1°	21.2
Soil sink	Output from the MeMo model based on Murguia-Flores et al. (2018, 2021). Data for the years 2019–2021 were set equal to 2017.	Monthly, with IAV	1°	-35.5
Total				548.9

References

Carbon Monitor. (2022). Retrieved May 1, 2022, from https://carbonmonitor.org/

Community Emissions Data System (CEDS). CEDS v_2021_04_21 gridded emissions data. (2021). Retrieved July 1, 2021, from https://data.pnnl.gov/dataset/CEDS-4-21-21

Crippa, M., Solazzo, E., Huang, G., Guizzardi, D., Koffi, E., Muntean, M., et al. (2020). High resolution temporal profiles in the Emissions Database for Global Atmospheric Research. *Scientific Data*, *7*(1), 121. https://doi.org/10.1038/s41597-020-0462-2

Etiope, G., Ciotoli, G., Schwietzke, S., & Schoell, M. (2019). Gridded maps of geological methane emissions and their isotopic signature. *Earth System Science Data*, *11*(1), 1–22. https://doi.org/10.5194/essd-11-1-2019

Gerlein-Safdi, C., & Ruf, C. S. (2019). A CYGNSS-Based Algorithm for the Detection of Inland Waterbodies. *Geophysical Research Letters*, *46*(21), 12065–12072. https://doi.org/10.1029/2019GL085134

Gerlein-Safdi, C., Bloom, A. A., Plant, G., Kort, E. A., & Ruf, C. S. (2021). Improving Representation of Tropical Wetland Methane Emissions With CYGNSS Inundation Maps. *Global Biogeochemical Cycles*, *35*(12), e2020GB006890. https://doi.org/10.1029/2020GB006890

Inoue, M., Morino, I., Uchino, O., Nakatsuru, T., Yoshida, Y., Yokota, T., et al. (2016). Bias corrections of GOSAT SWIR XCO_2 and XCH_4 with TCCON data and their evaluation using aircraft measurement data. *Atmospheric Measurement Techniques*, *9*(8), 3491–3512. https://doi.org/10.5194/amt-9-3491-2016

Lan, X., Thoning, K. W., & Dlugokencky, E. J. (2023). Trends in globally-averaged CH4, N2O, and SF6 determined from NOAA Global Monitoring Laboratory measurements. Version 2023-03. Retrieved from https://doi.org/10.15138/P8XG-AA10

Murguia-Flores, F., Arndt, S., Ganesan, A. L., Murray-Tortarolo, G., & Hornibrook, E. R. C. (2018). Soil Methanotrophy Model (MeMo v1.0): a process-based model to quantify global uptake of atmospheric methane by soil. *Geoscientific Model Development*, *11*(6), 2009–2032. https://doi.org/10.5194/gmd-11-2009-2018

Murguia-Flores, F., Ganesan, A. L., Arndt, S., & Hornibrook, E. R. C. (2021). Global Uptake of Atmospheric Methane by Soil From 1900 to 2100. *Global Biogeochemical Cycles*, *35*(7), e2020GB006774. https://doi.org/10.1029/2020GB006774

Parker, R. J., Webb, A., Boesch, H., Somkuti, P., Barrio Guillo, R., Di Noia, A., et al. (2020). A decade of GOSAT Proxy satellite CH_4 observations. *Earth System Science Data*, *12*(4), 3383–3412. https://doi.org/10.5194/essd-12-3383-2020

Saunois, M., Stavert, A. R., Poulter, B., Bousquet, P., Canadell, J. G., Jackson, R. B., et al. (2020). The Global Methane Budget 2000–2017. *Earth System Science Data*, *12*(3), 1561–1623. https://doi.org/10.5194/essd-12-1561-2020

Thoning, K. W., Tans, P. P., & Komhyr, W. D. (1989). Atmospheric carbon dioxide at Mauna Loa Observatory: 2. Analysis of the NOAA GMCC data, 1974–1985. *Journal of Geophysical Research: Atmospheres*, *94*(D6), 8549–8565. https://doi.org/10.1029/JD094iD06p08549

Tootchi, A., Jost, A., & Ducharne, A. (2019). Multi-source global wetland maps combining surface water imagery and groundwater constraints. *Earth System Science Data*, *11*(1), 189–220. https://doi.org/10.5194/essd-11-189-2019

Weber, T., Wiseman, N. A., & Kock, A. (2019). Global ocean methane emissions dominated by shallow coastal waters. *Nature Communications*, *10*(1), 4584. https://doi.org/10.1038/s41467-019-12541-7

van der Werf, G. R., Randerson, J. T., Giglio, L., van Leeuwen, T. T., Chen, Y., Rogers, B. M., et al. (2017). Global fire emissions estimates during 1997–2016. *Earth System Science Data*, *9*(2), 697–720. https://doi.org/10.5194/essd-9-697-2017

Xi, Y., Peng, S., Ducharne, A., Ciais, P., Gumbricht, T., Jimenez, C., et al. (2022). Gridded maps of wetlands dynamics over mid-low latitudes for 1980–2020 based on TOPMODEL. *Scientific Data*, *9*(1), 347. https://doi.org/10.1038/s41597-022-01460-w

Zheng, B., Chevallier, F., Yin, Y., Ciais, P., Fortems-Cheiney, A., Deeter, M. N., et al. (2019). Global atmospheric carbon monoxide budget 2000–2017 inferred from multi-species atmospheric inversions. *Earth System Science Data*, *11*(3), 1411–1436. https://doi.org/10.5194/essd-11-1411-2019